Journal of Geophysical Research: Atmospheres

RESEARCH ARTICLE
10.1029/2018JD028647

Vertical Profiles of Tropospheric Ozone From MAX-DOAS Measurements During the CINDI-2 Campaign: Part 1—Development of a New Retrieval Algorithm

Yang Wang[1], Janis Puķīte[1], Thomas Wagner[1], Sebastian Donner[1], Steffen Beirle[1], Andreas Hilboll[2], Mihalis Vrekoussis[2,3], Andreas Richter[2], Arnoud Apituley[4], Ankie Piters[4], Marc Allaart[4], Henk Eskes[4], Arnoud Frumau[5], Michel Van Roozendael[6], Johannes Lampel[7], Ulrich Platt[7], Stefan Schmitt[7], Daan Swart[8], and Jan Vonk[8]

[1]Max Planck Institute for Chemistry, Mainz, Germany, [2]Institute of Environmental Physics, University of Bremen, Bremen, Germany, [3]The Cyprus Institute, Nicosia, Cyprus, [4]Royal Netherlands Meteorological Institute, De Bilt, Netherlands, [5]Energy Research Centre of the Netherlands, Petten, Netherlands, [6]Royal Belgian Institute for Space Aeronomy – BIRA-IASB, Brussels, Belgium, [7]Institute of Environmental Physics, University of Heidelberg, Heidelberg, Germany, [8]National Institute for Public Health and the Environment, Bilthoven, Netherlands

Abstract Ground-based measurements of tropospheric ozone (O_3) are valuable for studies of atmospheric chemistry, air pollution, climate change, and for satellite validation. The Multi Axis Differential Optical Absorption Spectroscopy (MAX-DOAS) technique has been widely used to derive vertical profiles of trace gases and aerosols in the troposphere. However, tropospheric O_3 has not yet been satisfactorily derived from MAX-DOAS measurements due to the influence of stratospheric O_3 absorption. In this study, we developed two new retrieval approaches for tropospheric O_3 from MAX-DOAS measurements. In method 1, stratospheric O_3 profiles from external data sources are considered in the retrieval. In method 2, stratospheric and tropospheric O_3 are separated based on the temperature-dependent differences between tropospheric and stratospheric O_3 absorption structures in the UV spectral range. The feasibility of both methods is first verified by applying them to synthetic spectra. Then they are applied to real MAX-DOAS measurements recorded during the CINDI-2 campaign in Cabauw, the Netherlands (September 2016). The obtained results are compared with independent O_3 measurements and global chemical transport model simulations. Good agreement of the near-surface O_3 concentrations with the independent data sets is found for both methods. However, tropospheric O_3 profiles are only reasonably derived using method 1, while they are significantly overestimated at altitudes above 1 km using method 2, probably due to the approximation of the ring spectra used to correct the rotational Raman scattering structures in the DOAS fit. Advantages and disadvantages of both methods are discussed and improvement directions are suggested for further studies.

Key Points:
- Problems of MAX-DOAS retrievals of tropospheric O_3 are clarified and mostly solved
- New MAX-DOAS retrieval methods of vertical profiles of tropospheric O_3 are developed
- The feasibility of the new methods is proven and deficiencies are described for future research

Supporting Information:
- Supporting Information S1

Correspondence to:
Y. Wang,
y.wang@mpic.de

Citation:
Wang, Y., Puķīte, J., Wagner, T., Donner, S., Beirle, S., Hilboll, A., et al. (2018). Vertical profiles of tropospheric ozone from MAX-DOAS measurements during the CINDI-2 campaign: Part 1—Development of a new retrieval algorithm. *Journal of Geophysical Research: Atmospheres*, *123*, 10,637–10,670. https://doi.org/10.1029/2018JD028647

Received 12 MAR 2018
Accepted 10 AUG 2018
Accepted article online 21 AUG 2018
Published online 17 SEP 2018

Author Contributions:
Conceptualization: Yang Wang
Formal analysis: Yang Wang
Investigation: Yang Wang
Methodology: Yang Wang
Resources: Yang Wang
Writing - original draft: Yang Wang
Writing – review & editing: Yang Wang

1. Introduction

Ozone (O_3) plays an important role in controlling the tropospheric chemical composition, such as radicals, CO, CH_4, NO_x, halogen compounds, and hydrocarbons, through various reactions (Seinfeld & Pandis, 2016). Tropospheric O_3 also impacts the energy budget of the troposphere due to its absorption of thermal radiation (Seinfeld & Pandis, 2016). It is also a pollutant detrimental to human health and crop and ecosystem productivity. Previous studies showed that human activities significantly increased the tropospheric O_3 concentrations on a global scale. Even stronger enhancements are found on regional and local scales (Hough & Derwent, 1990; Logan, 1985). The increase of O_3 has drawn a lot of attention due to its role in the atmospheric chemistry, its harm to vegetation and human health, and its contribution to conversions of gas precursors into particles. Therefore, it is important to characterize the spatial and temporal variations of tropospheric O_3. And it is one of the key species in atmospheric chemistry models and model uncertainties can be largely reduced when measured ozone concentrations can be provided as input (Young et al., 2018).

Several kinds of in situ instruments have been developed to measure surface concentrations of ozone; they are mainly based on the following three techniques: chemiluminescence analyzers, devices measuring the ozone absorption in the UV, and a variety of wet-chemical sensors (Logan, 1985). Some of these techniques have been developed as commercial products and are widely used for operational monitoring and scientific

studies. Also, the long-path differential optical absorption spectroscopy (LP-DOAS) using an active light source, that is, a xenon lamp, has been widely used to measure the average of the O_3 concentration along a light path of several kilometers in the open atmosphere (Platt & Stutz, 2008).

Observing the vertical distribution of O_3 is more challenging than observing the surface concentrations. Ozone sondes (e.g., London & Liu, 1992) and airborne in situ instruments (e.g., Lenschow et al., 1980) are the traditional tools for such observations. However, the measurement frequency is limited due to the high operation costs. The differential absorption lidar (Browell, 1989) is the state-of-art technology to routinely measure vertical profiles of O_3 in an altitude range up to the tropopause with a high spatial and time resolution. A Tropospheric Ozone Lidar profiling Network (TOLNet) with six stations has been built in the United States in order to generate consistent and long-term data sets (Newchurch et al., 2016). However, the wide usage of this technique is also limited by the high costs of the instruments and their operation. In addition, an ozone lidar has a blind altitude interval near the surface which can be up to about 200 m depending on the individual instrumental properties (Newchurch et al., 2016).

The passive DOAS technique (Platt & Stutz, 2008) has been widely applied to analyze UV and visible spectra of direct and scattered sunlight observed from instruments operated at the ground, or on airborne and spaceborne platforms. From such observations, the spatial and temporal variation of atmospheric trace gases, for example, O_3, NO_2, SO_2, and HCHO, can be derived. The DOAS technique is based on the Lambert–Beer law, and for the data interpretation, usually radiative transfer models (RTM) are used. Total O_3 column densities have been derived from ground-based (e.g., Hendrick et al., 2011) and satellite DOAS instruments in the UV and visible spectral ranges (e.g., Eskes et al., 2005; Hoogen et al., 1999; McPeters et al., 1996; Veefkind et al., 2006). However, albeit progress in the retrieval of tropospheric O_3 vertical column densities (VCDs) or profiles were reported based on satellite measurements, that is, the OMI/MLS product (Ziemke et al., 2006), the accuracy of these products is still not fully satisfying, mainly due to the interference of the stratospheric O_3 absorption (Ziemke et al., 2006). Previous studies also reported on tropospheric O_3 retrievals from the Tropospheric Emission Spectrometer (TES) and Infrared Atmospheric Sounding Interferometer (IASI), both sensors operating in the thermal infrared spectral range (Oetjen et al., 2016, and references therein). However, the recent study by Neu et al. (2017) pointed out substantial differences in the tropospheric O_3 columns derived from different satellite instruments by up to 23%. Therefore, adequate means to accurately monitor the tropospheric O_3 columns from ground-based remote sensing techniques are needed for the validation of the satellite products and/or model simulations.

Multi Axis DOAS (MAX-DOAS) is a state-of-the-art ground-based remote sensing technique to retrieve vertical profiles and tropospheric columns of trace gases in the lower part of the troposphere (typically up to about 4 km) from spectra of scattered sunlight recorded at multiple elevation angles (Bobrowski et al., 2003; Hönninger & Platt, 2002; Hönninger et al., 2004; Wagner et al., 2004; Wittrock et al., 2004; Van Roozendael et al., 2004). In addition to the trace gas products, also profiles of aerosol extinction and the aerosol optical depth (AOD) can be retrieved from such measurements. MAX-DOAS instruments are relatively simple and cheap, and their operation can be performed automatically at rather low cost. In previous studies, MAX-DOAS measurements have successfully been applied to retrieve tropospheric columns, near-surface concentrations, and vertical profiles of NO_2, SO_2, HCHO, HONO, and CHOCHO, for which the tropospheric fraction is typically much larger than the stratospheric fraction. In contrast, the fraction of O_3 in the stratosphere is usually about 1 order of magnitude larger than that in the troposphere. Therefore, the retrieval of tropospheric O_3 from MAX-DOAS observations is still a challenge due to interference of the stratospheric O_3 absorption. One possible way to overcome the difficulty is to explicitly consider the stratospheric O_3 profiles in the tropospheric profiling algorithm. Information on stratospheric ozone profiles could be acquired from external climatology data sets, other measurements, and also from the zenith measurements of MAX-DOAS instruments themselves (e.g., Hendrick et al., 2011). Following this idea, Irie et al. (2011) assumed a fixed O_3 profile above 5 km in the inversion of tropospheric O_3 and included a factor in the fit to compensate for variations of the stratospheric O_3 column. Although their algorithm does not allow for a full vertical profile retrieval of tropospheric O_3 (only tropospheric O_3 VCDs and near-surface O_3 concentrations are retrieved), the retrieved near-surface O_3 concentrations were shown to be consistent with in situ measurements.

In this study, we developed a method to retrieve full profiles of tropospheric O_3 from MAX-DOAS measurements by including the stratospheric O_3 derived from a chemical model in the inversion scheme. However, one critical drawback of the method is its dependence on external data. Therefore, also a second method was developed which is based on the MAX-DOAS measurements only. Since the tropospheric and stratospheric temperatures are significantly different, the ozone absorptions in the two atmospheric layers can be separated by making use of the temperature dependence of the O_3 absorption in the UV spectral range, which has been used in Munro et al. (1998) to develop an algorithm of direct measurements of tropospheric ozone concentrations from Global Ozone Monitoring Experiment (GOME) satellite observations. In our study, in a first step, a set of synthetic spectra was generated using RTM simulations for different input O_3 profiles. The two methods are applied to the synthetic spectra, and the retrieved O_3 profiles are then compared to the "true" input O_3 profiles. From this comparison we assess the feasibility (and the uncertainties) of the two methods to retrieve the tropospheric O_3 profiles. The two retrieval methods are then applied to MAX-DOAS measurements taken during the CINDI-2 campaign (http://www.tropomi.eu/data-products/cindi-2; see section 2.1), in which several other independent measurements and model results of the surface concentration and vertical profiles of O_3 are available and can be compared to the MAX-DOAS results.

This paper is structured as follows: section 2 gives an overview of the CINDI-2 campaign, the MAX-DOAS measurements, and the independent data sets of O_3 available during the campaign. Also, simulations of synthetic spectra are described. In section 3, the details of the two retrieval methods are outlined. Their feasibility in accurately retrieving tropospheric ozone profiles is accessed by applying them to synthetic spectra in section 4. In section 5, the new retrieval methods are applied to MAX-DOAS measurements taken during the CINDI-2 campaign and the results are compared to those from independent techniques. In section 6, some important aspects causing potential significant error sources of the two methods are discussed. The error budgets of the retrieved tropospheric O_3 results are presented in section 7. The discussion and conclusions are presented in section 8.

2. Field Experiment and Generation of Synthetic Spectra

2.1. The CINDI-2 Campaign

The CINDI-2 campaign (Cabauw Intercomparison campaign of Nitrogen Dioxide measuring Instruments-2) was held in Cabauw (52°N, 5°E), the Netherlands, during September 2016 (http://www.tropomi.eu/data-products/cindi-2). The main objective of the campaign was the intercalibration of remote sensing instruments using the DOAS technique to monitor air quality and to validate satellite observations. More than 40 instruments operated by 30 groups participated in this field campaign. They include MAX-DOAS instruments as well as in situ systems and balloon sondes. The MPIC tube MAX-DOAS instrument also participated in this campaign, and its measurements during the period from 12 to 28 September, 2016, are used in this study.

2.1.1. The MPIC MAX-DOAS Instrument

A MAX-DOAS instrument (Donner, 2016) developed by the Max Planck Institute for Chemistry (MPIC), Mainz, Germany, was operated during the CINDI-2 campaign and the spectra it measured are used for this study. The instrument is referred to as MPIC "Tube MAX-DOAS" by the developers: its photograph is shown in the Figure S5 in the supporting information. The instrument contains outdoor and indoor parts. The outdoor part consists of a telescope which collects scattered sunlight, a motor which rotates the telescope, and an electric controlling unit mounted inside a plastic tube. The indoor part consists of the AvaSpec-ULS2048x64-USB2 spectrometer (https://www.avantes.com/products/spectrometers/sensline/item/817-avaspec-uls2048x64) with built-in CCD chip (charge coupled device) and a self-built Peltier temperature controlling container. The sunlight collected by the telescope is coupled into the spectrometer via a glass fiber bundle. The incident light first passes a slit, and then passes a Schott BG3 filter (https://www.itos.de/schott-optische-filter/bandpassfilter/bg3-bg25/) which filters the light above the wavelength of about 450 nm. Moreover, a special configuration with additional light traps added to the spectrometer was used. The spectrometer is a Czerny-Turner system and covers the wavelength range from 300 to 465 nm with a spectral resolution of around 0.6 to 0.7 nm full width at half maximum (FWHM) depending on the wavelength. The straylight level of the spectrometer given by the producer AVANTES Company is smaller than 0.4%. The temperature controlling unit stabilizes the temperature of the spectrometer to 20 °C with fluctuations of less than 0.1 °C. The instrument is automatically operated by computer software. Daytime measurements were routinely

performed for elevation angles of 1°, 2°, 3°, 4°, 5°, 6°, 8°, 15°, 30°, and 90° during the CINDI-2 campaign. The integration time of one spectrum was set to 1 min. The electric offset and dark current were corrected for each spectrum using the corresponding background measurements during nighttime. The slightly nonlinear response of the CCD of the spectrometer to the measured intensity (AVANTES Enlightening Spectroscopy, 2015) was corrected following the method from Horbanski (2016); details are given in Donner et al. (2015). The signal-to-noise ratio (SNR) of the instrument is around 3,000. More details of the MPIC Tube MAX-DOAS instrument are given in Donner (2016).

In order to separately compare the MAX-DOAS results with independent techniques under cloud-free and cloudy sky conditions, the sky conditions are automatically characterized from the MPIC MAX-DOAS observations themselves based on the MAX-DOAS cloud classification scheme (Wagner et al., 2014, 2016; Wang et al., 2015).

2.1.2. Independent Measurements of O_3

A Thermo 49i ozone analyzer (http://www.thermofisher.com/order/catalog/product/49I) was operated by the Energy Research Centre of the Netherlands. The instrument was located on the nearby 213-m-high (above ground level) meteorological tower of the Cabauw Experimental Site for Atmospheric Research (CESAR). The Thermo 49i provided the O_3 volume mixing ratios (VMRs) per half-hour at the altitudes of 20, 60, 120, and 200 m routinely by using gas inlets fixed at different altitudes of the tower. For the comparison with the MAX-DOAS results in section 5.2, the Thermo 49i measurements between the surface and 200 m were first interpolated onto a fine resolution grid with vertical steps of 20 m. Then the averaged O_3 VMRs in the layer from the surface to 200 m were derived based on the interpolated vertical profiles.

Another Thermo 49i in situ instrument operated by the National Institute for Public Health and the Environment (RIVM) measured the surface (3.5 m above ground level) O_3 concentration near the MPIC MAX-DOAS instrument with a high time resolution of 1 min. The hourly averaged data were used for the comparisons with the MAX-DOAS results in section 5.2.

A long-path DOAS (Pöhler et al., 2010) operated by the University of Heidelberg provided O_3 VMRs with a half-hour time resolution. In this system, one single telescope emitted and received the light from a xenon lamp. Four retro-reflectors were installed on the meteorological tower at different altitudes (13, 47, 107, and 207 m). The telescope was sequentially directed to the four reflectors in order to derive vertical profiles of trace gases in the layer below 200 m. The distance between the telescope and the reflectors was about 3.8 km resulting in a total atmospheric light path of 7.6 km. Averaged O_3 VMRs were derived from the retrieved profiles between the surface and 200 m for the comparison with the MAX-DOAS results in section 5.2.

Finally, a balloon sonde (a Science Pump Corporation (SPC) ECC ozone sensor coupled to a Vaisala RS92-SGP radiosonde) was regularly launched to measure the profile of O_3 concentrations from the surface up to 33 km. The measurements around noon were used for the comparisons with MAX-DOAS results in this study. There were two sonde measurements under cloud-free conditions during the period of our MAX-DOAS measurements: on 13 and 15 September 2016.

2.1.3. Chemical Transport Model Simulations

O_3 profiles during the campaign period were obtained from the ensemble system of the Copernicus Atmosphere Monitoring Service (CAMS; http://atmosphere.copernicus.eu/). The global (Inness et al., 2015) and the regional models (Marécal et al., 2015) of the CAMS system provide two sets of O_3 profile data, which are used for different purposes in this study. The model results are validated in Eskes et al. (2015). The CAMS global O_3 profiles are provided on 60 levels from the ground to about 64 km and on a horizontal grid of 0.4° by 0.4° with a time resolution of 3 h. The CAMS regional O_3 ensemble products are based on seven European-scale air quality models. The modeled O_3 profiles are provided on eight height levels up to 5 km and on a horizontal grid of 0.1° by 0.1° also with a time resolution of 3 h.

The stratospheric O_3 profiles from the CAMS global model are used in method 1 (see section 3.3) of the MAX-DOAS O_3 retrieval (section 5.1). The tropospheric O_3 profiles from the CAMS regional model ensemble are compared with the MAX-DOAS O_3 results (section 5.2). For comparisons with the MAX-DOAS measurements in section 5.2, the model data are interpolated to 1-hr steps.

Table 1
Parameters of the RTM Simulations for the Generation of Synthetic Spectra

RTM	SCIATRAN v3.6
Wavelength	310–360 nm
Spectral resolution	0.05 nm
Instrumental slit function	A Gaussian slit function with a FWHM of 0.5 nm
Temperature and pressure	One temperature and pressure profile as shown in Figure 1a
Considered trace gases	O_3, O_4, NO_2, HCHO, BrO, HONO
O_3 profile	Four O_3 profiles as shown in Figures 1c and 1d
Aerosols	Version 1: no aerosols Version 2: aerosol profile as shown in Figure 1b with AOD of 0.2, single scattering albedo of 0.92, and asymmetry factor of 0.68
Rotational Raman scattering	Version I: without rotational Raman scattering. Version II: with rotational Raman scattering
Viewing direction	Elevation angles: 1°, 2°, 3°, 4°, 5°, 6°, 8°, 15°, 30°, 90°One azimuth angle: 287°
Sun geometry	30 sun geometries for the conditions during the CINDI-2 campaign between 8:00 and 16:00 UTC on 14 September 2016:SZA between 50° and 70°; relative azimuth angle between 35° and 170°

2.2. Synthetic Spectra

It is difficult to quantitatively assess the performance of the MAX-DOAS O_3 results as the true O_3 values for the layers above 200 m are not known in the real measurements (except for the two ozone sonde measurements). Therefore, in order to verify the feasibility of the O_3 retrieval methods, we generated synthetic spectra in the wavelength range of 310–360 nm using simulations from the RTM SCIATRAN, version 3.6 (v3; 03 December 2015; Rozanov et al., 2014). The wavelength range is determined based on the requirement of method 2, namely, the considerable temperature dependence of O_3 absorption in the UV range (section 3.4). The parameters of the RTM simulations are listed in Table 1. The simulated synthetic spectra are convolved with a Gaussian slit function with a FWHM of 0.5 nm, which is similar to the slit function of the MPIC MAX-DOAS instrument during the CINDI-2 campaign. The synthetic spectra are simulated for the measurement geometries and Sun geometries of the MPIC MAX-DOAS measurements from 8:00 to 16:00 UTC on 14 September 2016. Fixed profiles of temperature and pressure (see Figure 1a), which were measured by the balloon sonde on 13 September, are used as input. Different O_3 profiles (see Figure 1c) are assumed below 4 km. The O_3 profile 1 (the black curve in Figure 1c) was measured by an ozone sonde on 13 September 2016. Above 4 km (Figure 1d), the same profile (also taken from the ozone sonde on 13 September 2016) is assumed for all the cases. Four sets of synthetic spectra are generated for the four ozone profiles in the atmosphere either including aerosols or not, and either considering the Rotational Raman Scatterings (RRS) or not. A typical aerosol extinction profile having an AOD of 0.2 (see Figure 1b) is assumed for the synthetic spectra with aerosols.

3. Development of Two Tropospheric O_3 Retrieval Methods

3.1. General Retrieval Approach of Vertical Profiles of Tropospheric Trace Gases

MAX-DOAS instruments measure spectra of the scattered sunlight at different elevation angles. The first step of the data analysis is the spectral analysis using the DOAS algorithm based on Lambert-Beer's law. As a result, the so-called slant column densities (SCDs) are retrieved from the measured spectra. The SCD is defined as the slant optical depth of a trace gas (depending on viewing geometry and solar position) normalized by its cross section, and is often interpreted (or approximated) as the integrated number density of a trace gas along the effective light path.

To analyze a measured spectrum I_m, a Fraunhofer reference spectrum (FRS) I_{FRS} is included in the DOAS fit as a reference spectrum:

$$\ln\left(\frac{I_m}{I_{FRS}}\right) = -\sigma\times(SCD_m - SCD_{FRS}) + \Sigma\left(\sigma_i'\times\left(SCD_{m_i}' - SCD_{FRS_i}'\right)\right) + P = -\sigma\times dSCD - \Sigma\sigma_i'\times dSCD_i' + P \quad (1)$$

where σ is the cross section of the trace gas of interest; σ_i' are cross sections of other trace gases in the same spectral range; SCD_m and SCD_{FRS} (SCD_{m_i}' and SCD_{FRS_i}') are the SCDs of the trace gas of interest (or the other trace gases) of the measured and the FRS spectra, respectively; and P represents the broadband

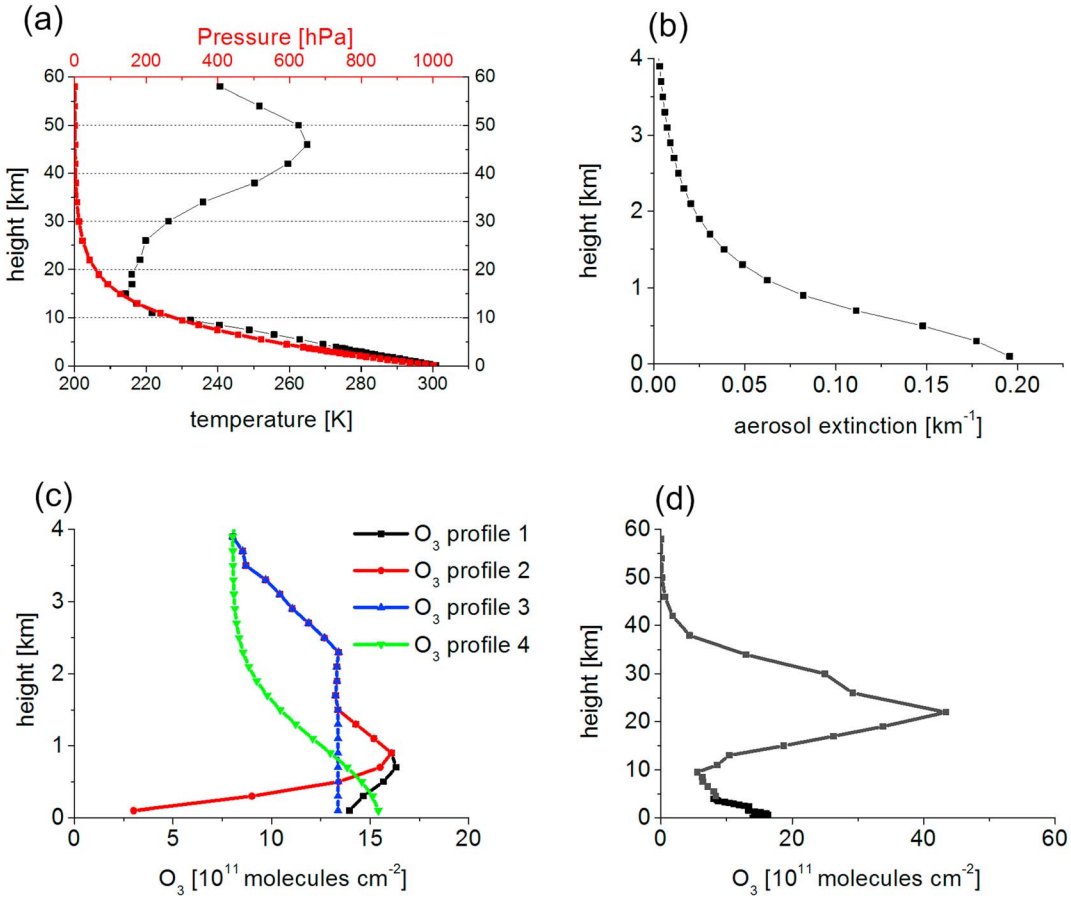

Figure 1. Profiles of (a) temperature and pressure, (b) aerosol extinctions, and (c) different ozone profiles below 4 km used for the RTM simulations. Above 4 km, the same O_3 profile (gray color in (d)) is used for all simulations.

absorptions and the effect of scattering by molecules and aerosols. From the DOAS fits the difference between SCD_m and SCD_{FRS} is retrieved, which is usually referred to as differential SCD (dSCD). For the trace gas of interest the dSCD is expressed by the following equation:

$$\mathrm{dSCD} = \int_{BOA}^{TOA} \mathrm{c(z)} \times dbAMF(z) \times dz \tag{2}$$

Here TOA and BOA are the top and bottom of the atmosphere, respectively. $c(z)$ is the concentration of the trace gas at the height z; dbAMF (z) is the altitude-dependent differential box air mass factor (Solomon et al., 1987):

$\mathrm{dbAMF\ (z) = bAMF_m\ (z) - bAMF_{FRS}\ (z)}$.

Here bAMF (z) represents the ratio of the effective light path length in an atmospheric layer divided by the vertical extension of that layer. bAMF (z) and dbAMF (z) can be simulated by a RTM.

The integral along altitudes in equation (2) (for our considerations) is separated in two parts, namely, for the tropospheric and stratospheric part:

$$\mathrm{dSCD} = \int_{BOA}^{tropopause} \mathrm{c(z)} \times dbAMF(z) \times dz + \int_{tropopause}^{TOA} \mathrm{c(z)} \times dbAMF(z) \times dz = dSCD_{Trop} + dSCD_{Stra} \tag{3}$$

Here $dSCD_{Trop}$ and $dSCD_{Stra}$ are partial dSCD of the trace gas in the troposphere and stratosphere, respectively.

If a spectrum measured in the zenith direction closest in time to the off-zenith measurements is used as I_{FRS}, such a FRS is referred to as "sequential FRS" in this study. For the zenith and off-zenith measurements at a

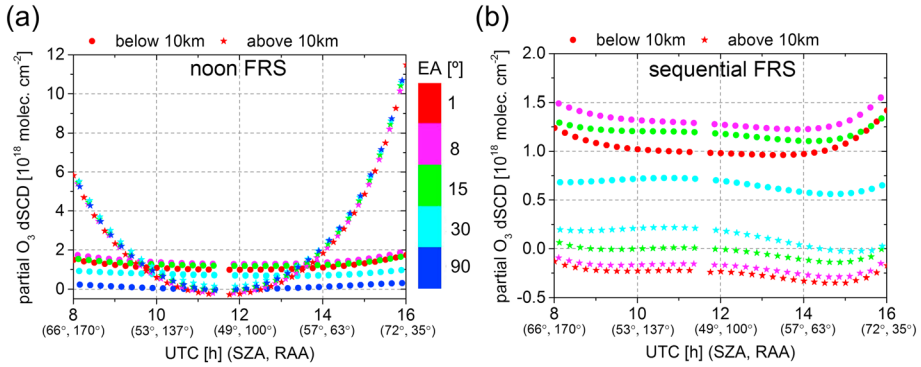

Figure 2. Tropospheric (below 10 km; circles) and stratospheric (above 10 km; stars) partial O_3 dSCDs for five elevation angles simulated by the RTM for a DOAS analysis with (a) a fixed (noon) FRS and (b) a sequential FRS. For the RTM the same input parameters as for the synthetic spectra are used (see text). Note that no O_3 dSCDs at 90° elevation are shown for the sequential FRS because they are zero by definition. The SZA and RAA are given in brackets below UTC time at the *x* axis.

close time with a similar solar zenith angle, light paths in the stratosphere between the zenith and off-zenith measurements are slightly different; thus, for trace gases mainly located in the troposphere, $dSCD_{Stra} \approx 0$. Therefore, based on equation (3), we can set

$$\mathrm{dSCD} \approx dSCD_{Trop} \tag{4}$$

The $dSCD_{Trop}$ can be approximately derived from the DOAS fit with the sequential FRS and is usually referred to as delta SCDs (Hönninger et al., 2004).

In the second step of the analysis, a vertical concentration profile of a trace gas c(z) in the troposphere is retrieved from the delta SCDs obtained from one elevation sequence of MAX-DOAS measurements by minimizing χ^2 in equation (5) using an inversion algorithm,

$$\chi^2 = \Sigma\left(\mathrm{dSCD}_i - \widehat{\mathrm{dSCD}}_i\right)^2 \tag{5}$$

i indicates the elevation angle in one elevation sequence; $\widehat{\mathrm{dSCD}}$ is simulated by a RTM for a given c(z). For this task, two methods are used by different groups: the so-called optimal estimation retrievals (Clémer et al., 2010; Frieß et al., 2006, 2011; Hartl & Wenig, 2013; Irie et al., 2008, 2011; Rodgers, 2000; Wittrock, 2006; Wang et al., 2013a, 2013b, 2017; Yilmaz, 2012) and parameterized retrievals based on look-up tables (Li et al., 2010, 2013; Vlemmix et al., 2010, 2011; Wagner et al., 2011). The optimal estimation algorithm will be used in this study. The vertical integration of retrieved profiles yields the tropospheric VCD of the trace gas.

3.2. Effects of Stratospheric O_3 on the Retrieval of Tropospheric O_3 Profiles

The typical retrieval approach described in section 3.1 works well for trace gases which are mainly located in the troposphere. However, for O_3, the stratospheric VCD is typically about 1 order of magnitude larger than that in the troposphere (see the O_3 profile measured by the ozone sonde shown in Figure 1d). Therefore, the approximation in equation (4) is inappropriate, and even a small relative error of the stratospheric dSCD directly leads to large errors of the tropospheric results. Thus, the stratospheric dSCDs have to be quantified individually for each measurement.

In order to quantify the fractions of the O_3 $dSCD_{Stra}$ and $dSCD_{Trop}$ we run the RTM SCIATRAN v3 to simulate them with the same input RTM parameters as those for the synthetic spectra (the case with aerosols and using O_3 profile 1). We assume that the tropopause is located at 10 km. Since in previous studies typically a fixed FRS was used (instead of a sequential FRS), the RTM simulations are done for both options using either a fixed (noon) FRS (shown in Figure 2a) or a sequential FRS (shown in Figure 2b). Figure 2 indicates that $dSCD_{Stra}$ is strongly reduced by using a sequential FRS compared to a fixed FRS. However, even for the analysis with sequential FRS, it is found that the $dSCD_{Stra}$ is

still as large as about 30% of the $dSCD_{Trop}$. These findings clearly indicate that the effect of the stratospheric O_3 absorption needs to be exactly considered for the retrieval of tropospheric O_3 even if a sequential FRS is used in the DOAS fits. Here it is important to mention that the substantial values of O_3 $dSCD_{Stra}$ for the sequential FRS are not caused by the temporal evolution of the $dSCD_{Stra}$ during the period of the elevation scan, because the sequential FRS is derived by interpolating the zenith measurements from the beginning to the end of each elevation sequence to exactly match the time of individual off-zenith measurements. This procedure is used in all simulations and retrievals for the analysis with a sequential FRS in this study. The considerable O_3 $dSCD_{Stra}$ is due to the remaining differences of the light paths between the off-zenith and zenith view and the significant O_3 amount in the stratosphere.

There are two methods which are developed in this study to quantify and correct for the stratospheric O_3 dSCD in the retrieval of tropospheric O_3: in method 1, $dSCD_{Stra}$ is calculated for each measurement based on stratospheric O_3 profiles derived from external sources. In method 2, the O_3 $dSCD_{Stra}$ (and $dSCD_{Trop}$) are determined in the DOAS fit based on the temperature dependence of O_3 absorptions. The O_3 $dSCD_{Trop}$ derived from the two methods can subsequently be used to retrieve vertical profiles of tropospheric O_3 using a profile inversion algorithm similar to those for other tropospheric species. The theoretical derivations of both methods are described in sections 3.3 and 3.4.

It is also worth mentioning that in the case of a strongly absorbing species like ozone the light path integral formalism used in equation (2) and the following equations is fundamentally overestimating the effects due to nonlinearity (Puķīte & Wagner, 2016) and thus provides an error source. Although not explicitly quantified, this inaccuracy competes with and contributes to the observed discrepancies and is implicitly accounted for in the error budget estimation.

3.3. Method 1: Use of External Data Sets of Stratospheric O_3

Considering the rather high proportions of the O_3 $dSCD_{Stra}$ in the total O_3 dSCD retrieved from MAX-DOAS measurements with the sequential FRS, in order to compensate the O_3 $dSCD_{Stra}$ for the retrieval of tropospheric O_3, it is an obvious approach to quantify the O_3 $dSCD_{Stra}$ based on a stratospheric O_3 profile acquired from external data sets. Stratospheric O_3 profiles can be obtained from other measurements, chemical model simulations, climatological data sets, and eventually also from zenith-sky observations of the MAX-DOAS measurements at twilight (e.g., Hendrick et al., 2011). In this study the stratospheric O_3 profiles (above 10 km) are taken from the CAMS global model (see section 2.1.3). The stratospheric O_3 profile at the time closest to the individual MAX-DOAS measurement is used.

The external stratospheric O_3 profiles can be used to calculate O_3 $dSCD_{Stra}$ based on equation (3). The dbAMF for the calculations need to be simulated by a RTM for each MAX-DOAS measurement. Note that aerosols corresponding to each MAX-DOAS measurement should also be considered in the RTM simulations of stratospheric dbAMF. O_3 dSCDs are retrieved from MAX-DOAS measured spectra using DOAS fits with the sequential FRS. Then the O_3 $dSCD_{Stra}$ is subtracted from the derived O_3 dSCD to acquire the O_3 $dSCD_{Trop}$. The O_3 $dSCD_{Trop}$ in one elevation sequence are finally used to retrieve profiles of tropospheric O_3 by minimizing

$$\chi^2 = \Sigma\left(\mathrm{dSCD}_{Trop_i} - \widehat{\mathrm{dSCD}}_{Trop_i}\right)^2 \tag{6}$$

Equation (6) is adapted from equation (5), but is now applied to the tropospheric partial columns.

3.4. Method 2: Separation of the Stratospheric and Tropospheric O_3 dSCD Based on the Temperature Dependence of the O_3 Absorption

In this section, we describe a newly developed method to separate O_3 $dSCD_{Stra}$ and $dSCD_{Trop}$ in the DOAS fits. This method does not depend on external data sets of stratospheric O_3 profiles which are needed for the first method. Instead, it utilizes the temperature dependence of the O_3 absorption.

Serdyuchenko et al. (2014) measured O_3 cross sections in the laboratory for the temperature range from 193 to 293 K in 10-K steps. These measurements and also many other previous studies demonstrate that the O_3 cross sections in the Huggins bands (about 310–350 nm) significantly depend on

temperature. For a temperature change from 203 to 273 K, the absolute values of the O_3 cross section vary by 30 to 70%, depending on the wavelength (Serdyuchenko et al., 2014, and references therein). The Chappuis band in the visible spectral range of about 400–800 nm is also often used for remote sensing of O_3, but unlike the Huggins bands, the temperature dependence of the O_3 Chappuis bands is only up to 1% (Serdyuchenko et al., 2014). Thus, method 2 is applied for the measurements in the Huggins bands.

In the following, we use effective O_3 cross sections calculated for specific temperatures. This concept was already applied for the retrieval of the total O_3 VCD from satellite measurements of GOME (Hoogen et al., 1999), OMI (Veefkind et al., 2006), and SCIAMACHY (Eskes et al., 2005) as well as for separating stratospheric and tropospheric NO_2 in ground-based direct Sun measurements (Spinei et al., 2014). The calculation of an O_3 cross section for an effective temperature (referred to as effective O_3 cross section (σ_e) in the following) is outlined below.

For O_3, substituting dSCD in equation (1) with equation (2),

$$\ln\left(\frac{I_m}{I_{FRS}}\right) = \left[-\int_{BOA}^{TOA}\sigma(T(z))\times dbAMF(z)\times c(z)\times dz\right] - \sum\sigma_i^{'}\times dSCD_i^{'} + P \tag{7}$$

Here $\sigma(T(z))$ is the O_3 cross section at the height z with the temperature T (z).

If the total O_3 absorption is represented by an effective O_3 cross section (σ_e), equation (7) can be written as

$$\ln\left(\frac{I_m}{I_{FRS}}\right) = \left(-\sigma_e\times\int_{BOA}^{TOA} dbAMF(z)\times c(z)\times dz\right) - \sum\sigma_i^{'}\times dSCD_i^{'} + P \tag{8}$$

σ_e is derived from the equivalence of equation (7) with equation (8):

$$\sigma_e = \frac{\int_{BOA}^{TOA}\sigma(T(z))\times dbAMF(z)\times c(z)\times dz}{\int_{BOA}^{TOA} dbAMF(z)\times c(z)\times dz} \tag{9}$$

Similarly, effective O_3 cross sections for the troposphere (σ_{e_Trop}) and stratosphere (σ_{e_Stra}) can be defined as follows:

$$\sigma_{e\_Trop} = \frac{\int_{BOA}^{tropopause}\sigma(T(z))\times dbAMF(z)\times c(z)\times dz}{\int_{BOA}^{tropopause} dbAMF(z)\times c(z)\times dz} \tag{10}$$

$$\sigma_{e\_Stra} = \frac{\int_{tropopause}^{TOA}\sigma(T(z))\times dbAMF(z)\times c(z)\times dz}{\int_{tropopause}^{TOA} dbAMF(z)\times c(z)\times dz} \tag{11}$$

Here we use the database of O_3 cross sections from Serdyuchenko et al. (2014), because it covers the largest temperature range available in the literature so far. However, the temperature step of 10 K provided by the Serdyuchenko database is too coarse for our needs. Therefore and also to smooth out artifacts at individual temperatures, the empirical Bass-Paur parameterization (Paur & Bass, 1985) of the temperature dependence of the O_3 cross sections by a second-order polynomial is used to derive the O_3 cross section at a specific temperature from the Serdyuchenko database:

$$\sigma(\lambda) = C_0(\lambda) + C_1(\lambda)\times T + C_2(\lambda)\times T^2 \tag{12}$$

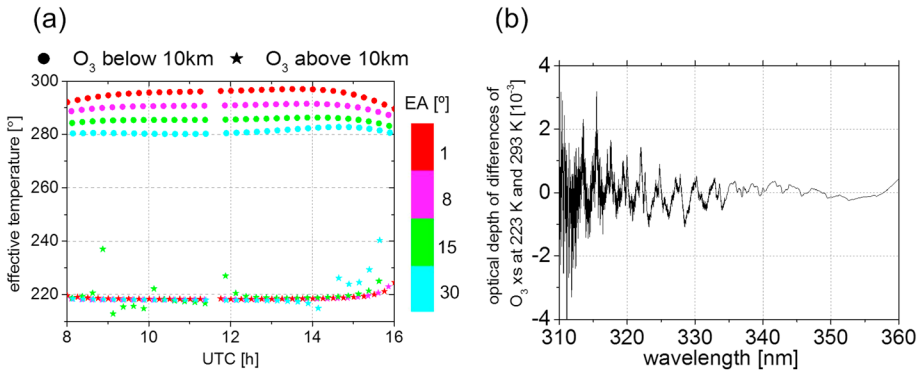

Figure 3. (a) Effective temperatures of the tropospheric (below 10 km, circles) and stratospheric (above 10 km, starts) O_3 for different elevation angles calculated for the synthetic spectra (with aerosols and for the O_3 profile 1). (b) Optical depths of narrowband spectral differences of the O_3 cross sections at 223 and 293 K for an assumed O_3 dSCD of 1×10^{18} molecules/cm^2.

Here $C_0(\lambda)$, $C_1(\lambda)$, and $C_2(\lambda)$ are wavelength-dependent fit coefficients, which can be derived from the Serdyuchenko O_3 cross sections. Serdyuchenko et al. (2014) demonstrate that the precision of the parameterization is generally within 2% and the parameterized cross section has a better signal-to-noise ratio compared to the original cross sections at individual temperatures, because artifacts from measurements at single temperatures are partly smoothed out.

With σ_{e_Trop} and σ_{e_Stra}, the integral in equation (8) is substituted by the $dSCD_{Trop}$ and $dSCD_{Stra}$ based on equation (3),

$$\ln\left(\frac{I_m}{I_{FRS}}\right) = -\left(\sigma_{e\_Trop}\times dSCD_{Trop} + \sigma_{e\_Stra}\times dSCD_{Stra}\right) - \Sigma\sigma_i^{'}\times dSCD_i^{'} + P \tag{13}$$

If the σ_{e_Trop} is sufficiently different from σ_{e_Stra}, the $dSCD_{Trop}$ and $dSCD_{Stra}$ can be retrieved from the spectrum in the DOAS fit. By this procedure O_3 in the troposphere and the stratosphere are treated as two different species because of their different absorption structures. The $dSCD_{Trop}$ from one elevation sequence can finally be used in the tropospheric O_3 profile retrieval by minimizing χ^2 in equation (6). Differently from method 1, no external data set of stratospheric O_3 is needed in method 2. However, the feasibility of method 2 depends on the differences of σ_{e_Trop} and σ_{e_Stra} and how well the corresponding spectral features can be separated in the DOAS analysis. Their differences depend on the effective temperatures of O_3 in the troposphere (T_{e_trop}) and stratosphere (T_{e_stra}). We estimated both effective temperatures for the MAX-DOAS measurements during the CINDI-2 campaign and investigated the corresponding differences of the spectral structures of σ_{e_Trop} and σ_{e_Stra}.

Similar with equations (10) and (11), T_{e_trop} and T_{e_stra} are calculated as follows:

$$T_{e\_trop} = \frac{\int_{BOA}^{tropopause} T(z)\times dbAMF(z)\times c(z)\times dz}{\int_{BOA}^{tropopause} dbAMF(z)\times c(z)\times dz} \tag{14}$$

$$T_{e\_stra} = \frac{\int_{tropopause}^{TOA} T(z)\times dbAMF(z)\times c(z)\times dz}{\int_{tropopause}^{TOA} dbAMF(z)\times c(z)\times dz} \tag{15}$$

T_{e_trop} and T_{e_stra} are calculated for the synthetic spectra (with aerosols and for the O_3 profile 1) and shown in Figure 3a. dbAMFs for the calculations are simulated by the RTM SCIATRAN v3 with the same input as for the

simulations of the synthetic spectra. The height of the tropopause is assumed to be 10 km. T_{e_stra} and T_{e_trop} are about 220 K and between 280 and 300 K (depending on elevation angle), respectively. Their difference is about 70 K, which should be sufficient to separate the tropospheric and stratospheric O_3 dSCDs. The considerable dependences of T_{e_trop} on the elevation angle and Sun geometry demonstrate the need to calculate σ_{e_Trop} and $\sigma_{e_Stra}$for individual measurements.

Because the DOAS fit is sensitive to the narrow spectral structures of the cross sections, the differences of the narrow spectral structures of the O_3 cross sections between 293 and 223 K in the wavelength range of 310–360 nm are extracted and shown in Figure 3b. The differences are derived through fitting the O_3 cross section at 290 K by that at 220 K and a third-order polynomial. The residual structure of the fit represents the differences of the narrow spectral structures between both cross sections. When the residual structure is multiplied by a typical tropospheric O_3 dSCD of 1×10^{18} molecules/cm^2, it yields the typical optical depth (OD) corresponding to the differences of the O_3 absorptions at both temperatures. The residual structure has a peak amplitude of about 2×10^{-3} and is thus larger than a typical fit residual of the MPIC MAX-DOAS instrument of about 5×10^{-4} (see Figure 8). Moreover, it has a pronounced systematic structure, whereas a typical fit residual contains mainly noise. Based on these findings we expect that the narrow spectral structures of the differences between the two effective O_3 cross sections can in principle be well identified in the spectral analysis of our MAX-DOAS measurements during the CINDI-2 campaign. In Figure 3b it can also be seen that the largest differences are found below 335 nm. Thus, we selected 340 nm as the upper limit of the spectral range used for the O_3 analysis. Since the SNR of the MAX-DOAS spectra strongly decreases below 320 nm, this wavelength was chosen as the lower limit of the spectral range used for the O_3 analysis. In addition, it needs to be noted that the amplitude of the differences of both effective O_3 cross sections is 1 order smaller than the amplitude of one O_3 cross section. Therefore, we expect that the measurement noise might still lead to rather large relative fit errors if two cross sections for different effective temperatures are included in the DOAS fit (the detailed discussion is in section 6.2.3).

4. Feasibility Test of the Two Retrieval Methods Based on Synthetic Spectra

In this section we test the feasibility of both methods to retrieve tropospheric O_3 profiles based on synthetic spectra. The tests have been conducted for the four chosen sets of synthetic spectra either with or without aerosols and with or without RRS (see section 2.2 and Table 1). In section 4.1, the O_3 $dSCD_{Trop}$ using both methods retrieved from the synthetic spectra are compared to the "true" values, which are simulated by the RTM. In section 4.2, the tropospheric O_3 profiles retrieved from either the analysis of the synthetic spectra or the O_3 $dSCD_{Trop}$ simulated by the RTM are compared to the true O_3 profiles (input profiles for the simulations of the synthetic spectra). The tropopause is assumed at 10 km in this section to be consistent with the analysis of the real measurements (section 5).

4.1. Retrieval of Tropospheric O_3 dSCDs

dbAMFs are needed for many steps of the different retrievals (e.g., the calculation of the true O_3 $dSCD_{Trop}$, the calculation of the O_3 $dSCD_{stra}$ in method 1, or the calculation of the effective O_3 cross sections in method 2), which are simulated by the RTM SCIATRAN v3 with the same input parameters for the simulations of the synthetic spectra. The simulations are done at the "effective wavelength" of the O_3 AMF in the DOAS fits and in the spectral range of 320–340 nm. Based on previous studies (e.g., Marquard et al., 2000), the effective wavelength for that spectral range is around 325 nm. Thus, this wavelength is used in the following. However, it must be noted that the actual effective wavelength varies along changes of ozone absorptions, measurement geometries, and other atmospheric properties. This effect can contribute to the differences between retrieved O_3 values and the true values at 325 nm. In addition, the typical uncertainties of bAMFs are about 5% and depend on altitude, measurement geometry and solar geometry, aerosol scenario, and other atmosphere and surface scenarios (Wagner et al., 2007). One uncertainty source of bAMFs, which considerably impacts method 1, is discussed in section 6.2.3.

In the next step, the synthetic spectra are analyzed with the QDOAS software (http://uv-vis.aeronomie.be/software/QDOAS/; Danckaert et al., 2017) using a sequential FRS. The parameters of the DOAS fit are listed in Table 2. For method 1, two O_3 cross sections at 223 and 293 K are included in the DOAS fit. The sum of the fit coefficients of both O_3 cross sections represents the total O_3 dSCD. Then $dSCD_{stra}$

Table 2
DOAS Analysis Settings of Tropospheric O_3 dSCDs for the Synthetic Spectra and the MPIC MAX-DOAS Measurements

Parameter	Synthetic spectra	MPIC MAX-DOAS measurements
Fitting spectral range	320–340 nm	√
Wavelength calibration	Taken from the inputs	Calibration based on Fraunhofer lines of Kurucz solar spectrum (Kurucz, 1984)
Slit function	A Gaussian slit function with a FWHM of 0.5 nm	A slit function measured by a mercury lamp at 334 nm with a FWHM of about 0.64 nm
Cross sections		
O_3	Method 1: cross sections (Serdyuchenko et al., 2014) at 223 and 293 K, dSCD is the sum of the fit coefficients for the two cross sections. Method 2: σ_{e_Trop} and σ_{e_Stra} calculated for individual spectra with the temperature and O_3 profiles assumed for the synthetic spectra based on the literature cross sections (Serdyuchenko et al., 2014). Additional settings: I_0 correction[a] (10^{20} molecule/cm^2); linear and square Taylor terms of the two cross sections (see Puķīte et al., 2010)	Method 1: √ Method 2: σ_{e_Trop} and σ_{e_Stra} calculated for individual spectra with the fixed O_3 profile (the O_3 profile 1 in Figure 1c) and the temperature profiles derived from the hourly averaged surface temperatures Additional settings: √
NO_2	Vandaele et al. (1998), 298 K, I_0-corrected[a] (10^{17} molecules/cm^2)	√
O_4	Thalman and Volkamer (2013), 293 K	√
HCHO	Meller and Moortgat (2000), 297 K	√
Ring effect	Exact Ring spectra (see section 6.2.1)	Normal Ring spectrum calculated based on Kurucz solar atlas and an additional Ring scaled with $(\lambda/354\ \text{nm})^4$ (Wagner et al., 2009)
Intensity offset	No	Polynomial of order 1 (corresponding to two coefficients) in intensity space
Polynomial term	Polynomial of order 3 (corresponding to six coefficients)	√
Wavelength adjustment	All spectra are shifted and stretched against FRS	√
Fraunhofer reference spectrum (FRS)	Sequential FRS	√

Note. √ indicates that the item for the MPIC MAX-DOAS measurements is same as that for the synthetic spectra.
[a]Solar I_0 correction (Aliwell et al., 2002).

is calculated for each synthetic spectrum based on equation (3) and subtracted from the retrieved total O_3 dSCD to acquire the O_3 $dSCD_{Trop}$. For method 2, the σ_{e_trop} and σ_{e_stra} are calculated for individual spectra with the temperature and O_3 profiles assumed in the RTM simulations of the synthetic spectra. For both methods, in order to approximately account for the effect of the wavelength dependence of the dSCD (Marquard et al., 2000; Puķīte et al., 2010; Richter, 1997, and references therein), a linear term ($\lambda \times \sigma$) and a square term (σ^2) of both effective O_3 cross sections are also included in the DOAS fit according to the so-called Taylor series approach (TSA) developed by Puķīte et al. (2010). Other absorbers, NO_2, O_4, and HCHO are also included in the DOAS fit. For the synthetic spectra including RRS, spectra for the correction of the Ring effect have to be included. Usually, a so-called Ring spectrum is used for that purpose, which is a first-order approximation of the Ring effect (Chance & Spurr, 1997; Grainger & Ring, 1962; Shefov, 1959; Solomon et al., 1987; Wagner et al., 2009). However, it is clear that especially for measurements with a strong influence of RRS, such a Ring spectrum cannot exactly correct for the Ring effect. Therefore, alternatively an "exact" Ring spectrum (see section 6.2.1) can be derived from the synthetic spectra calculated with and without RRS. Note that exact Ring spectra are calculated individually for the DOAS analysis of each synthetic spectrum. For the synthetic spectra without RRS, no Ring spectra are included in the DOAS fit. To account for the stray light in the measured spectra, normally, a nonlinear fit implemented in the intensity space is included in the DOAS fit, referred to as the intensity offset correction. However, because stray light contamination is not an issue for the synthetic spectra, no intensity offset correction is applied. Additionally, we test the effect of including an intensity offset corrections on the retrieved O_3 dSCDs. It can change the retrieved O_3 dSCD by about 2% for method 1 and 6% for method 2, respectively. These tests are used in the evaluations of the error budget in section 7.1. Although variations of the wavelength calibration do not occur for the synthetic spectra, the wavelength adjustment is still allowed in the DOAS fits to compensate for the tilt effect (Lampel et al., 2017).

The relative differences of O_3 $dSCD_{Trop}$ retrieved from the synthetic spectra using both methods compared to the true values are plotted in Figure 4 for the four assumed O_3 profiles and three selected elevation angles. The comparison results for the synthetic spectra with and without aerosols are shown in Figures 4a and 4b, respectively. The comparison results for the synthetic spectra with and without RRS are marked by the solid and dashed curves in the subfigures of Figure 4. In general, the deviations of the retrieved O_3 $dSCD_{Trop}$ from the true values are smaller than 5% for method 1, and smaller than 10% for method 2. Generally, larger deviations (up to 30%) are found for the synthetic spectra with RRS than those without RRS, especially for the spectra without aerosols and at low elevation angles. And this finding is more obvious for method 2 than for method 1. The most probable explanation for these findings are the interferences of the exact Ring structures with the O_3 absorption structures in the DOAS fit, because the fit coefficient of the exact Ring ranges between 0.7 and 1 depending on sun and measurement geometries. A more detailed discussion of this effect is given in section 6.2.1. For the synthetic spectra without RRS, deviations of the retrieved O_3 $dSCD_{Trop}$ from the true values are still considerable with a maximum of 10%, depending on the observation geometry. This finding might be due to the dependence of the effective AMF-wavelength on the observation geometry and the nonlinear effects of the ozone absorption on the light paths (Puķīte & Wagner, 2016).

4.2. Retrieval of Tropospheric O_3 Concentration Profiles

The profile inversion algorithm is applied to the $dSCD_{Trop}$ derived from the synthetic spectra to retrieve tropospheric O_3 profiles, which are then compared with the true profiles used as input for the synthetic spectra. In this study we use the PriAM profile inversion algorithm (Wang et al., 2013a, 2013b, 2017), which is based on the optimal estimation method. The PriAM algorithm was verified in several studies (e.g., Frieß et al., 2016; Wang et al., 2017). The dbAMF and $\widehat{\mathrm{dSCD}}_{Trop}$, which are needed for the profile inversion, are calculated online by PriAM using the SCIATRAN RTM version 2.2 (v2; Rozanov et al., 2005). Aerosol scenarios consistent with those used in the simulation of the synthetic spectra are included in the retrieval. For PriAM, an a priori profile with a constant value of 6×10^{11} molecules/cm^3 from the surface up to 10 km is used. The diagonal elements of the covariance matrix of the a priori uncertainty (S_a) are set to the square of 20% of the a priori profile, and the nondiagonal elements are calculated using the Gaussian function with the correlation height (CH) of 1 km from the diagonal elements. The effects of the a priori profile and S_a on the profile retrieval are discussed in Text S1 in the supporting information. Based on these results optimal settings are chosen. The diagonal elements of the covariance matrix of the measurement uncertainties (S_m) are set to 10% of the tropospheric O_3 dSCDs, according to the typical SNR of the MPIC MAX-DOAS measurements, and the nondiagonal elements are set to 0. The O_3 $dSCD_{Trop}$ simulated by the RTM SCIATRAN v3 and retrieved from the individual sets of synthetic spectra using method 1 and method 2 (all shown in Figure 4) are input in the PriAM profile inversion.

The retrieved profiles for one MAX-DOAS elevation sequence at 12:00 UTC are compared with the true (input) profiles in Figure 5. The results indicate that the four different O_3 profiles can be generally well reproduced by the retrievals with the different input O_3 $dSCD_{Trop}$. The profiles retrieved from the O_3 $dSCD_{Trop}$ simulated by the RTM SCIATRAN v3 ($Profile_{SCI\_v3}$; cyan curves in Figure 5) are more consistent with the true values than the profiles retrieved using the O_3 $dSCD_{Trop}$ retrieved from the synthetic spectra, especially than those retrieved with method 2 (with RRS) and without aerosols (blue curves in Figure 5). This finding is consistent with the deviations of the retrieved $dSCD_{Trop}$ from the true dSCDs shown in Figure 4. The diurnal variation of the differences of the retrieved profiles from the true profiles is shown in Figures 6b and 6c. The diurnal variation of the true profiles (constant values) is also shown in Figure 6a for a comparison with Figures 6b and 6c. Because the results in Figure 5 indicate that the O_3 profiles retrieved from the different sets of $dSCD_{Trop}$ are quite similar with the $profile_{SCI\_v3}$, only the results for $profile_{SCI\_v3}$ are shown in Figures 6b and 6c. The deviations of $profile_{SCI\_v3}$ from the true profiles can be attributed to the inconsistency of the simulations of O_3 $dSCD_{Trop}$ and dbAMF between the different versions of the RTM SCIATRAN (v3 and v2). Here it should be noted that SCIATRAN v2 is used by PriAM. Another reason for the differences might be remaining artifacts of the PriAM inversion algorithm.

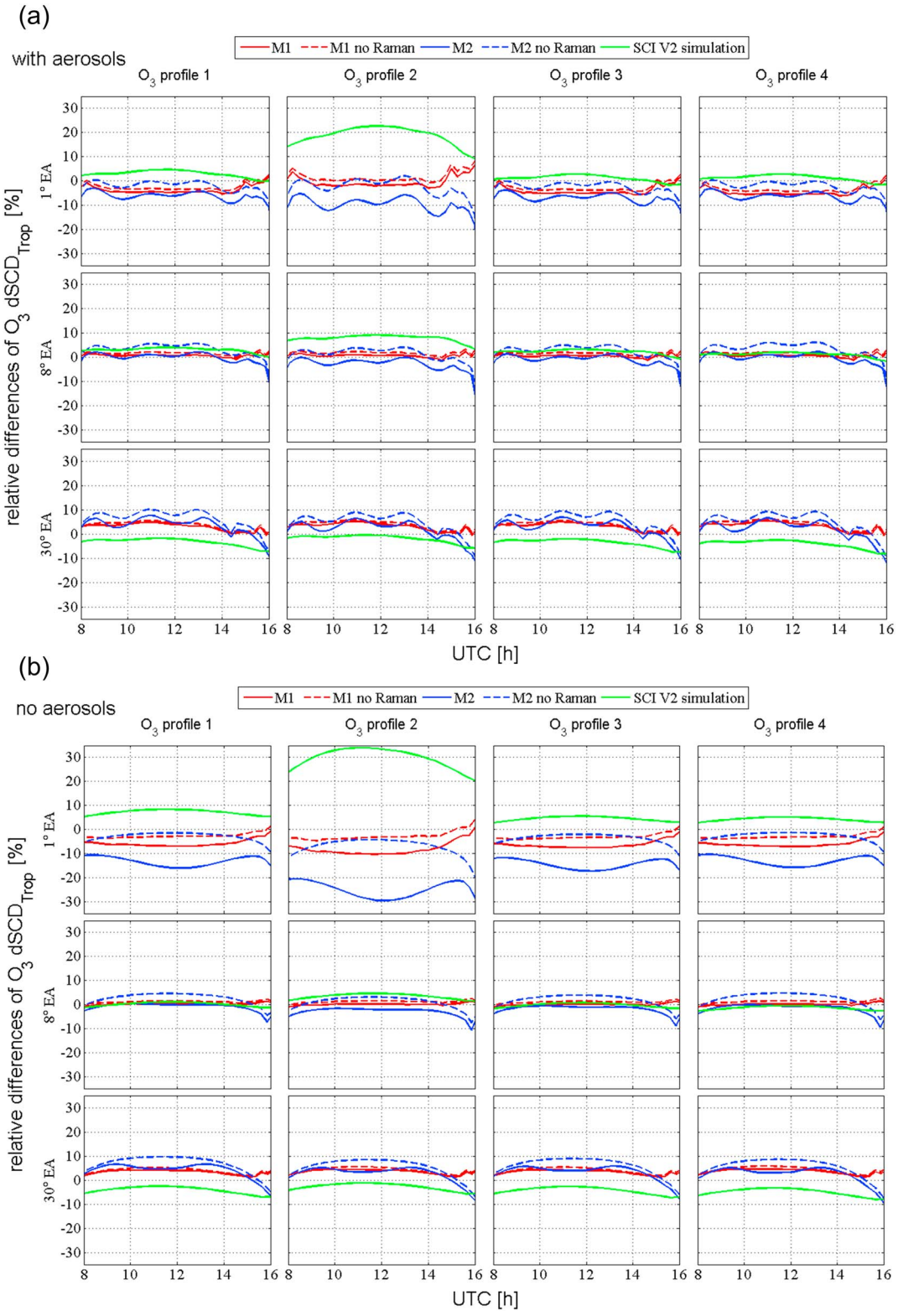

Figure 4. Relative differences of the tropospheric O_3 partial dSCDs ($dSCD_{Trop}$) retrieved from the synthetic spectra and true values simulated by RTM (SCIATRAN v3). (a) Results for the synthetic spectra with aerosols. (b) Results for the synthetic spectra without aerosols. In each subfigure, the $dSCD_{Trop}$ retrieved using method 1 and method 2 are marked by red and blue colors, respectively. The retrieved $dSCD_{Trop}$ for the synthetic spectra with and without RRS are plotted as solid and dashed curves, respectively. Different rows and columns of the subfigures show results for three elevation angles and four different O_3 profiles shown in Figure 1c. The green curves denote the relative differences of the $dSCD_{Trop}$ simulated by the RTM SCIATRAN v2 compared to those by the RTM SCIATRAN v3.

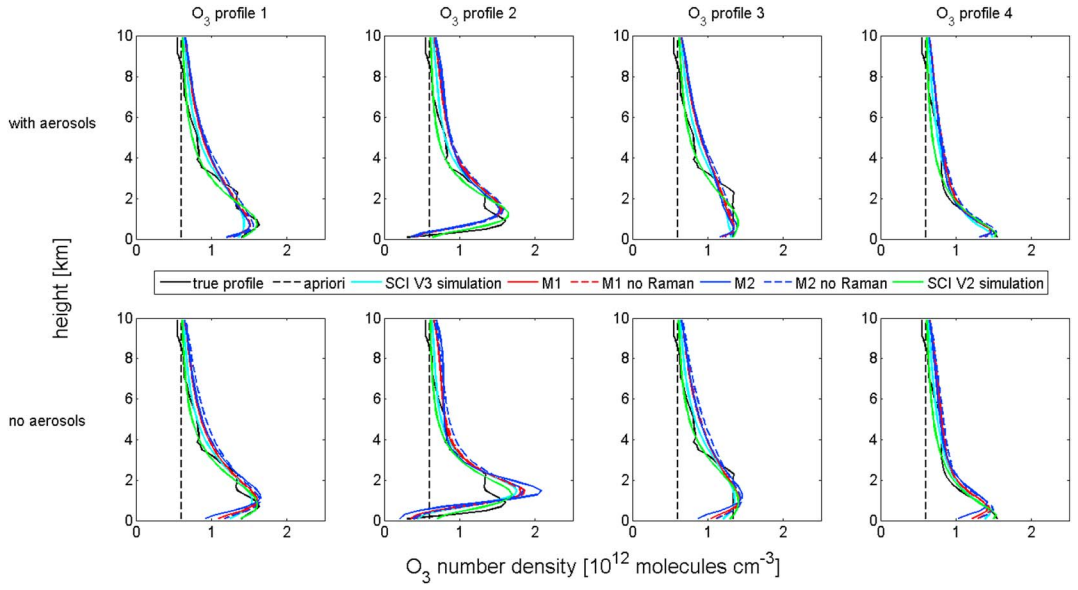

Figure 5. Retrieved profiles (color curves) from the tropospheric O_3 dSCDs shown in Figure 4 at 12:00 UTC for synthetic spectra (top) with aerosols and (bottom) without aerosols. Different columns of the subfigures are for the four assumed O_3 profiles. Green and cyan curves are the retrieved profiles from the tropospheric O_3 dSCDs simulated by the RTM SCIATRAN v2 and v3, respectively. Red and blue solid (dashed) curves are the retrieved profiles from the synthetic spectra with (without) the RRS using method 1 and method 2, respectively. The assumed true O_3 profiles and the a priori O_3 profile for the profile inversions are shown as black solid and dashed curves in the individual subfigures.

In order to interpret the deviations of the $profile_{SCI\_v3}$ from the true values, we simulate the O_3 $dSCD_{Trop}$ for the same scenarios as for the synthetic spectra using the SCIATRAN RTM v2. Afterward, the simulated O_3 $dSCD_{Trop}$ are used as input to retrieve the tropospheric O_3 profiles ($profile_{SCI\_v2}$). The $profile_{SCI\_v2}$ are shown as green curves in Figure 5. The diurnal variation of the differences of $profile_{SCI\_v2}$ from the true values is shown in Figure 6. The deviations of $profile_{SCI\_v2}$ from the true values can only be attributed to the artifacts of the PriAM inversion algorithm. Figures 5 and 6 indicate that $profile_{SCI\_v2}$ is not much different from $profile_{SCI\_v3}$. Only the values of $profile_{SCI\_v2}$ below and above 2 km are slightly larger and smaller than the corresponding values of $profile_{SCI\_v3}$ by up to $\pm 1 \times 10^{11}$ molecules/cm^3 (about 7% in the altitudes below 4 km). $Profile_{SCI\_v2}$ is closer to the true values than $profile_{SCI\_v3}$.

These findings are consistent with the differences of the O_3 $dSCD_{Trop}$ between both RTM versions shown in Figure 4, which indicates that the O_3 $dSCD_{Trop}$ simulated by SCIATRAN v3 are smaller and larger than simulated by SCIATRAN v2 at low- and high-elevation angles, respectively. The differences of $profile_{SCI\_v2}$ from the true values in Figures 5 and 6 indicate that the steep gradient of the profiles around 2 km cannot be well retrieved due to the limited sensitivity of MAX-DOAS measurements at high altitudes. An exemplary averaging kernel (AK) for the O_3 profile retrieval is shown in Figure 7, indicating that the retrieval is only sensitive to altitudes below 2 km typically. Similar AKs are also obtained for the real MPIC MAX-DOAS measurements during the CINDI-2 campaign. In addition, Figure 5 indicates that the retrieved profiles above 2 km are well consistent with the true values, although the retrieval sensitivity is quite low as shown by the AKs in Figure 7. This finding indicates that some information on O_3 at altitudes above 2 km can still be derived from the measurements. The main reasons for this are that (a) the high-elevation angles are still sensitive for these layers and (b) the ozone mixing ratio at altitudes above 2 km typically does not vary strongly. Thus, even with the limited information content of the measurement, the average O_3 mixing ratio in the free troposphere can be constraint. However, as shown in the paper, the information is quite limited, and the retrieval works well only for the synthetic spectra. For the real measurements, shortcomings of the retrieval and/or measurement noise can degenerate retrievals of O_3 profiles above 2 km. Moreover, if the O_3 profiles are significantly different from the a priori profiles, it is expected that the profiles are not able to be well retrieved. In addition, in Figure 6, relatively large deviations of the retrieved profiles from the true profiles are found in the morning and in

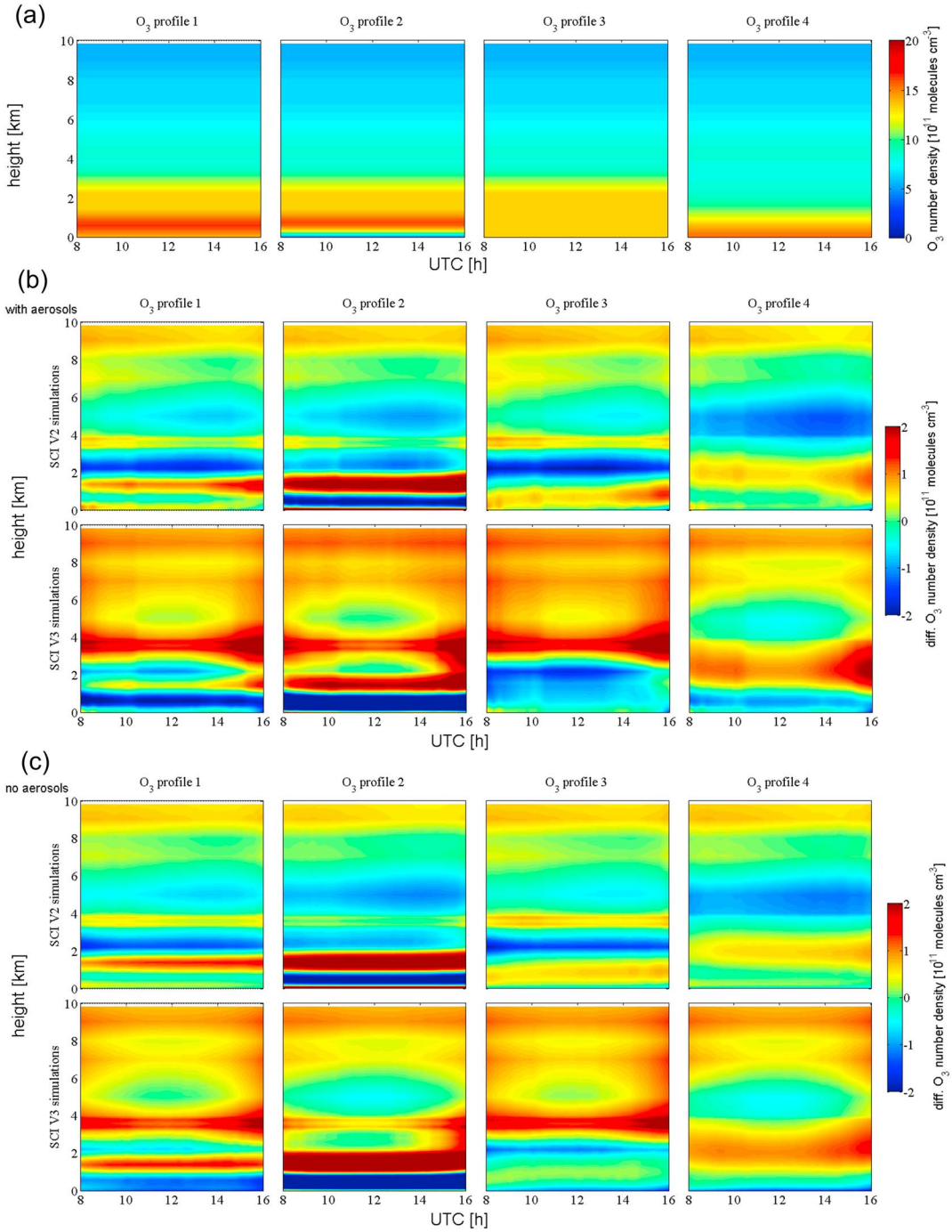

Figure 6. (a) Diurnal variation of "true" O_3 profiles and differences of profiles retrieved from simulated $dSCD_{Trop}$ and the true profiles for the scenarios (b) with and (c) without aerosols. Different columns of the subfigures show results for the four assumed O_3 profiles. The first and second rows in (b) and (c) represent results for O_3 $dSCD_{Trop}$ simulated by the RTM SCIATRAN v2 and v3, respectively.

the afternoon, with larger deviations in the afternoon when the RAA between the viewing direction and the Sun is small. This effect is stronger for the results retrieved from the O_3 $dSCD_{Trop}$ simulated by SCIATRAN v3 than v2. The effect for SCIATRAN v2 is mainly due to artifacts of the PriAM profile inversion. A lower degree of inversion freedom is found in the afternoon. The effect for SCIATRAN v3 is mainly due to discrepancies between both RTM versions, and the discrepancies could be larger at a larger SZA and a smaller RAA. In

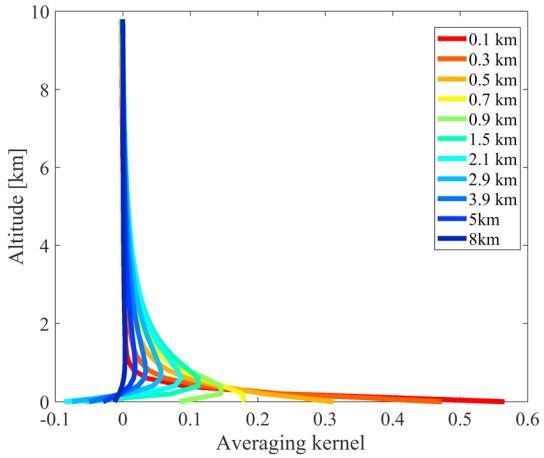

Figure 7. Typical averaging kernels of tropospheric O_3 profile retrievals for different altitudes of the derived O_3 profile for a measurement at a SZA of about 50°. The number of degree of freedom is 1.5.

general, the tropospheric O_3 profile can be well retrieved from the O_3 $dSCD_{Trop}$ below 2 km. The retrieval errors can be attributed to errors of the $dSCD_{Trop}$, inconsistencies between both RTM, and artifacts of the profile inversion algorithm. The error of the retrieved O_3 number density can be up to 2×10^{11} molecules/cm^2 at altitudes where steep gradients of the O_3 concentration occur.

In addition to the tropospheric profiles, the tropospheric O_3 VCD can be derived by integration of the profiles. The VCDs derived from the different sets of retrieved profiles are compared to the true VCDs in Figure S6 in the supporting information. For the profile$_{SCI_v2}$ and profile$_{SCI_v3}$, and the profiles retrieved from the synthetic spectra using both methods, the relative differences of the VCDs from the true values are generally smaller than 2, 5, and 10%, respectively.

5. Retrieval of Tropospheric O_3 From Real MAX-DOAS Measurements and Comparison With Independent Techniques

In this section both methods described above are applied to measurements of the MPIC MAX-DOAS instrument during the CINDI-2 campaign. In section 5.1 the retrieval of the O_3 $dSCD_{Trop}$ using a sequential FRS is discussed. Afterward, the tropospheric O_3 profiles retrieved from the two data sets of O_3 $dSCD_{Trop}$ using both methods are discussed and compared with independent measurements in section 5.2. In addition, the aerosol profiles, which are needed for the retrieval of the O_3 $dSCD_{Trop}$ and tropospheric O_3 profiles, are derived from the MAX-DOAS measurements of the oxygen dimer (O_4) using the PriAM profile inversion algorithm.

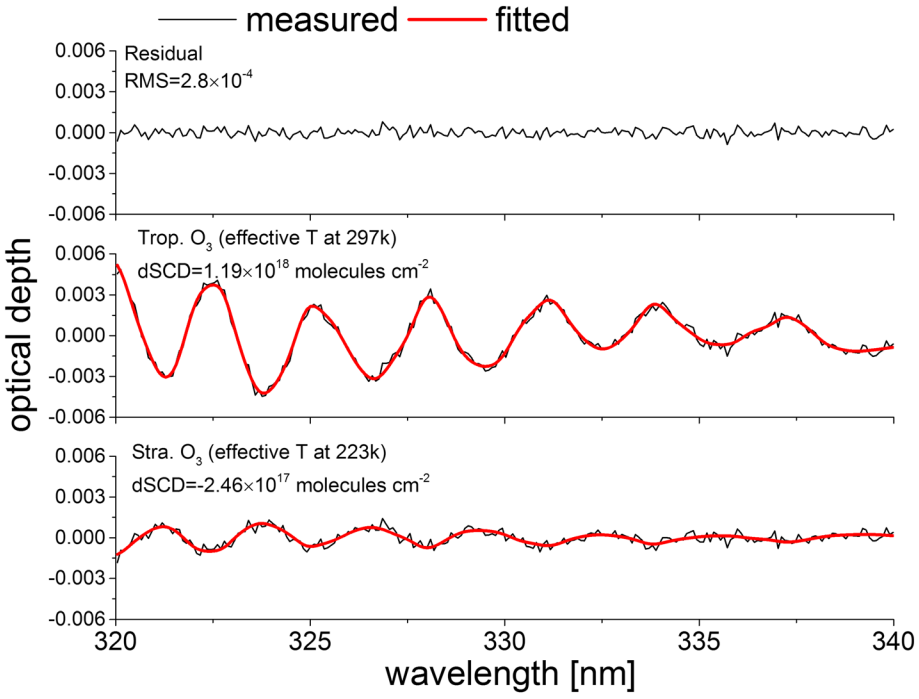

Figure 8. Example of a DOAS fit of a measured spectrum (elevation angle of 1° at 8:00 UTC on 14 September 2016) using a sequential FRS. The residual structures and the corresponding RMS are shown in the top figure. The derived absorption structures of the tropospheric O_3 and stratospheric O_3 are shown in the middle and bottom figures, respectively. The effective temperatures for the effective tropospheric and stratospheric cross sections are about 297 and 223 K, respectively. Note that the differential O_3 cross sections are used in the DOAS fit along with their linear and square Taylor terms (see Table 2) orthogonalized to them.

Single scattering albedo (SSA) and asymmetric parameter (g) of the aerosols are set as 0.92 and 0.68, respectively, based on measurements of a Sun photometer near the MAX-DOAS instrument.

5.1. Retrieval of Tropospheric O_3 dSCDs From Real Measurements

O_3 $dSCD_{Trop}$ are retrieved from individual MPIC MAX-DOAS measurements during the CINDI-2 campaign using sequential FRS. The parameters of the DOAS fits of measured spectra are shown in Table 2. For both methods many of the parameters are the same, but different O_3 cross sections are used. For method 1, the O_3 cross sections at 223 and 293 K are used to retrieve the total O_3 dSCD, from which the O_3 $dSCD_{stra}$ is subtracted to acquire the O_3 $dSCD_{Trop}$. The O_3 $dSCD_{stra}$ is individually calculated for each measurement using the RTM-simulated stratospheric dbAMFs and the stratospheric O_3 profiles based on equation (3). To be consistent with the RTM used in the PriAM profile inversion algorithm, the RTM SCIATRAN v2 is also used to simulate dbAMFs for the calculations of O_3 $dSCD_{stra}$. In the simulation of the stratospheric dbAMFs, the aerosol profiles retrieved from each MAX-DOAS measurements are taken into account. Because of the considerable variations of the stratospheric O_3 during the campaign (see section 6.1.1), the stratospheric O_3 profiles from the CAMS global model closest in time to the MPIC MAX-DOAS measurements are used in the calculations. For method 2, two effective O_3 cross sections (σ_{e_Trop} and σ_{e_Stra}) are calculated for individual measurements according to equations (10) and (11) and are included in the DOAS fit. dbAMFs are simulated for individual measurements using the RTM SCIATRAN v2 with the aerosol profiles retrieved from the MAX-DOAS measurements. Considering the variation of surface ambient temperature of up to 20 K during the campaign and the substantial temperature dependence of the retrieved O_3 $dSCD_{Trop}$ (see Text S2 in the supporting information), atmospheric temperature profiles below 10 km are calculated from the hourly averaged surface temperature by assuming a lapse rate of 0.645 K per 100 m. Above 10 km a fixed temperature profile (the average of the balloon sonde measurements during the CINDI-2 campaign) is used. One important aspect needs to be mentioned: possible temperature inversion layers in the boundary layer are not considered in the proposed procedure. This simplification can contribute to errors of the retrieved Trop. O_3 dSCD of up to 10% s if inversion layers with 10-K temperature difference were present (see the sensitivity tests in S2 in the supporting information). However, temperature inversion layers did not occur often based on the sonde measurements. Therefore, these effects have probably a minor importance in this study. However, it could be critical in locations where diurnal variations of surface temperatures are strong and inversion layers occur often. As shown in Text S2 in the supporting information, the determination of O_3 $dSCD_{Trop}$ using method 2 is not sensitive to changes of the tropospheric O_3 profile which is assumed for the calculation of σ_{e_Trop}. Therefore, one fixed O_3 profile, which is derived from the measurement of the ozone sonde on 13 September 2016, is used for the calculation of σ_{e_Trop} in all retrievals. The tropopause, which is the altitude at which tropospheric and stratospheric O_3 are separated, is set to 10 km for all retrievals. The selection of this altitude is based on two aspects: first, at midlatitudes the tropopause is usually located around 10 km. Second, the dbAMFs change from positive to negative values in the altitude range of 5–10 km. Thus, if a lower separation altitude is used, the calculated stratospheric effective cross sections can reach extreme unphysical values due to the competition between the positive and negative dbAMF at different altitudes. In such cases, also outliers and large scatter of the retrieved O_3 $dSCD_{Trop}$ and O_3 $dSCD_{stra}$ are often found. This effect is discussed in detail in Text S3 in the supporting information. It must be noted that it is not necessary to account for the exact height of the tropopause in the retrievals. The retrieval results are representative for a tropopause height at 10 km for all retrievals. The retrieved O_3 $dSCD_{Trop}$ can change by up to 5% if the tropopause height is varied by about ±2 km.

One example of a DOAS fit with both effective O_3 cross sections for an elevation angle of 1° at 8:00 UTC on 14 September is shown in Figure 8. The absorption structures of the two effective O_3 cross sections are well fitted and are substantially larger than the fit residual. The retrieved O_3 $dSCD_{Trop}$ using both methods on 14 September 2016, which is a totally cloud-free day, are shown in Figure 9. In general, the O_3 $dSCD_{Trop}$ retrieved from both methods are mostly in the range of 1 to 1.5×10^{18} molecules/cm^2. However, significant differences are found for both results. Stronger scatter of O_3 $dSCD_{Trop}$ and larger O_3 $dSCD_{Trop}$ at large elevation angles are found for method 2 compared to method 1. These differences are most probably caused by the effect of a nonperfect correction of the Ring effect and noise on the results of method 2 (see section 6.2). For method 1 a strong increase of the O_3 $dSCD_{Trop}$ in the afternoon after 15:00 UTC when the RAA is small can be seen. This finding is probably caused by errors of RTM simulations for such small scattering angles (see section 6.1.2), and instrumental effects, for instance, stray light.

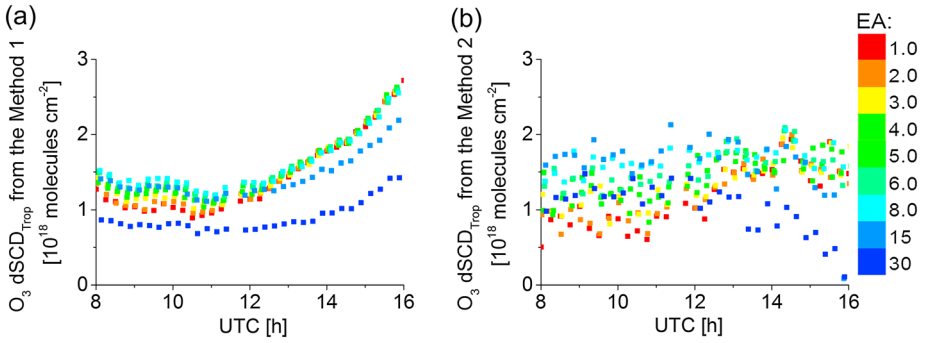

Figure 9. Tropospheric O_3 dSCDs retrieved from the MPIC MAX-DOAS instrument on 14 September 2016 using a sequential FRS using (a) method 1 and (b) method 2. The colors denote the elevation angles.

5.2. Comparisons With Independent Measurements

From the two sets of O_3 $dSCD_{Trop}$ retrieved using the two methods, the corresponding tropospheric O_3 profiles are retrieved for the measurements during the whole campaign. In the profile inversion, the same a priori profile and uncertainty covariance (S_a) as for the inversion of the synthetic spectra are used. As diagonal elements of S_m the fit errors of the O_3 $dSCD_{Trop}$ are used and the nondiagonal elements are set to 0. The aerosol profiles obtained by the MAX-DOAS measurements are used for the O_3 profile inversion. An example of the retrieved O_3 profiles for 14 September 2016 (totally cloud free) is shown in Figure 10. The results for the O_3 $dSCD_{Trop}$ retrieved using method 1 and method 2 are shown in the top panels of Figures 10a and 10b, respectively. O_3 profiles obtained by the CAMS regional model on the same day are shown in Figure 10c for comparisons with the MAX-DOAS results. Note that the profiles from the CAMS regional model are available only up to 5 km. The comparison indicates that the diurnal variations of the O_3 profiles from method 1 are more consistent with the model results before 14 UTC than those from method 2. The O_3 number densities in the altitude range between 2 and 6 km for method 2 are much larger than those for method 1 and the CAMS regional model by up to ~1×10^{12} molecules/cm^3 (about 100% at 4-km altitude). This finding is related to the larger O_3 $dSCD_{Trop}$ for large-elevation angles for method 2 than for method 1 (see section 5.1 and Figure 9). However, the diurnal variation of the O_3 profiles below 2 km for method 2 is generally consistent with the CAMS results. In addition, the O_3 number densities in the altitude range between 2 and 6 km after 15 UTC for method 1 are much larger than those for method 2 and the CAMS results. This finding is related to the strong increase of the O_3 $dSCD_{Trop}$ for method 1 (see section 5.1 and Figure 9). In Figure 10 also the measured and simulated O_3 $dSCD_{Trop}$ by the PriAM algorithm are shown. In general, both sets of O_3 $dSCD_{Trop}$ are well reproduced by the PriAM algorithm, but also systematic differences are found. In general, the simulated O_3 $dSCD_{Trop}$ are smoother than the measured ones obtained from method 2. For method 1, the large O_3 $dSCD_{Trop}$ at 30° elevation in the afternoon cannot well be reproduced by PriAM. However, even if the simulated O_3 $dSCD_{Trop}$ would better match the measured ones, this would not improve the agreement of the derived O_3 profiles with the CAMS model results, because the corresponding profiles would have even higher O_3 VMRs at high altitudes. Note that O_3 $dSCD_{Trop}$ is innerly simulated by the SCIATRAN RTM in the retrieval of O_3 profiles by a use of the PriAM algorithm.

The retrieved O_3 VMRs in the lowest layer of 0–200 m are compared with the results from independent techniques, including a Thermo 49i ozone analyzer, a long-path DOAS, an in situ instrument operated by the national air quality monitoring network of RIVM, and the CAMS model simulations (see section 2.1.2). These data sets are averaged over each hour for the comparisons. The comparison results on 14 September 2016 are shown in Figure 11, indicating a generally consistent diurnal variation. We further compare the near-surface results for the whole campaign. The comparisons are done for cloud-free and cloudy conditions in Figures 12a and 12b, respectively. For the comparison, the data from the Thermo 49i ozone analyzer with gas inlets at different altitudes and from the LP-DOAS with reflectors at different altitudes of the tower are converted to the average O_3 VMRs in the altitude range of 0–200 m to be as consistent as possible with the MAX-DOAS results. The details of the conversion are given in section 2.1.2. The correlation coefficients (R) of MAX-DOAS results with different O_3 data under cloud-free conditions are generally around

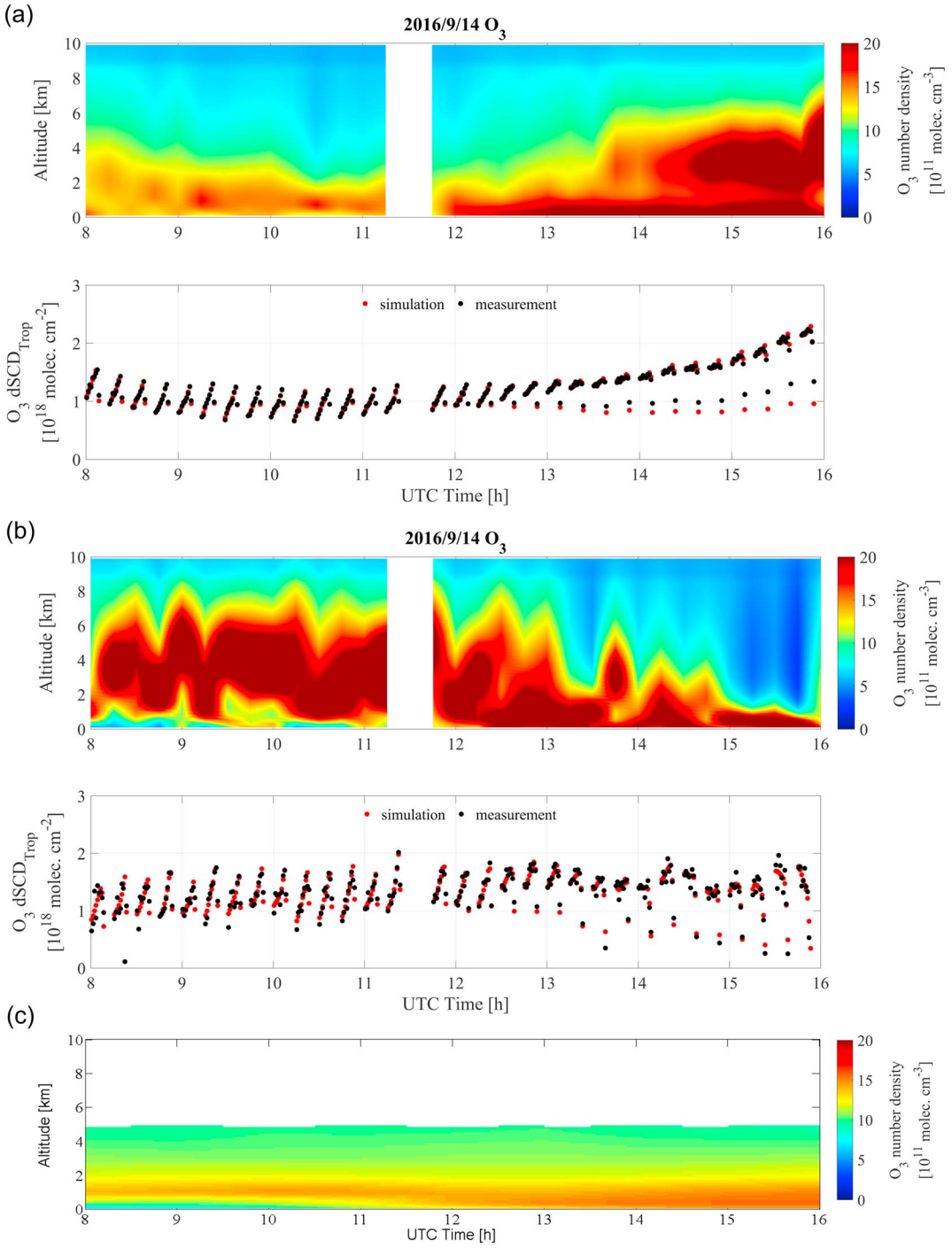

Figure 10. Time series of tropospheric O_3 profiles retrieved from the MPIC MAX-DOAS measurements on 14 September 2016 based on the O_3 $dSCD_{Trop}$ retrieved using either (top panel in a) method 1 or (top panel in b) method 1. The measured and simulated O_3 $dSCD_{Trop}$ of the profile retrievals are shown in the bottom panels in (a) and (b). The tropospheric O_3 profiles derived from the CAMS regional model are shown in (c).

0.8, which is much better than those found under cloudy conditions. The MAX-DOAS results are generally 10% larger than the other data probably due to the different altitude range for which the MAX-DOAS measurements are sensitive. Under cloud-free conditions, the systematic deviations of the results from method 2 compared to the other data are smaller than that for method 1. This finding is probably caused

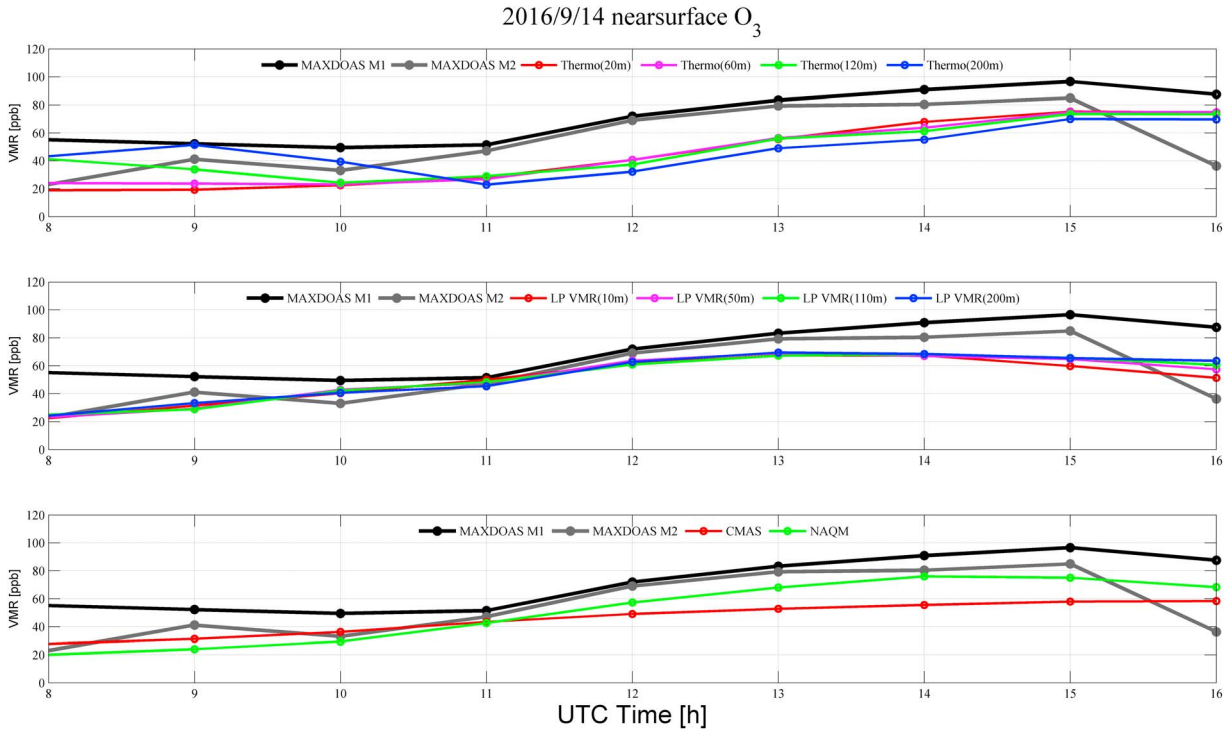

Figure 11. Comparison of the O_3 VMRs in the lowest profile grid (0–200 m) retrieved from the MPIC MAX-DOAS measurements using method 1 (black curves) and method 2 (gray curves) with near-surface O_3 VMRs derived from other techniques (colored curves) on 14 September 2016. (top) O_3 VMRs measured by a Thermo 49i ozone analyzer with the gas inlets at different altitudes of 20, 60, 120, and 200 m on the tower. (middle) O_3 VMRs measured by a LP-DOAS instrument with reflectors at altitudes of 10, 50, 110, and 200 m. (bottom) Averaged O_3 VMRs in the altitude ranges of 0–200 m derived from the CAMS model and surface O_3 VMRs measured by a Thermo 49i ozone analyzer operated by NAQM.

by errors of the RTM simulations of the O_3 $dSCD_{Stra}$ for method 1 (see section 6.1.2). However, under cloudy conditions, the results from method 1 are much more consistent with the other data than those from method 2. This implies that clouds can significantly impact the separations of the two effective O_3 in the DOAS fit of method 2. Additional errors arise from the cloud effect on the bAMF and thus also on the calculation of the effective O_3 cross sections. Finally, clouds have a strong effect on the radiative transfer in the troposphere, which is not covered by the RTM. However, this effect will have similar influence on the results of both methods.

The retrieved O_3 profiles from the MAX-DOAS measurements are compared with the measurements of the ozone sonde and the results of the CAMS regional model on the two days with the ozone sonde measurements (both under cloud-free conditions) in Figure 13. The MAX-DOAS results and CAMS model simulations are averaged for 2 hr around the ozone sonde measurements. Generally, the MAX-DOAS O_3 profiles retrieved using method 1 agree well with the ozone sonde measurements and the model results. In contrast, MAX-DOAS O_3 concentrations retrieved using method 2 are much larger than those for method 1 and the other independent data sets above 1 km (similar as in Figure 10). This finding is directly related to the overestimation of the O_3 $dSCD_{Trop}$ for large elevation angles by method 2 (see section 5.1 and Figure 9). A detailed discussion on the phenomenon is given in section 6.2.2. In addition, Figure 13 indicates that the MAX-DOAS O_3 results for method 1 are systematically lower than the ozone sonde measurements at altitudes above 1 km. This finding can probably be attributed to the lower sensitivity of the MAX-DOAS measurements to higher altitudes (see the typical AK in Figure 7). Although the effect also plays a role for method 2, it is not visible because the overestimation of O_3 $dSCD_{Trop}$ for large elevation angles is dominant.

We also compare the O_3 number densities retrieved from MAX-DOAS with those of the CAMS regional model at different altitudes up to 4 km for the whole campaign. Only cloud-free conditions are selected. From the comparisons, the correlation coefficients (R), slopes, intercepts, and mean relative differences are

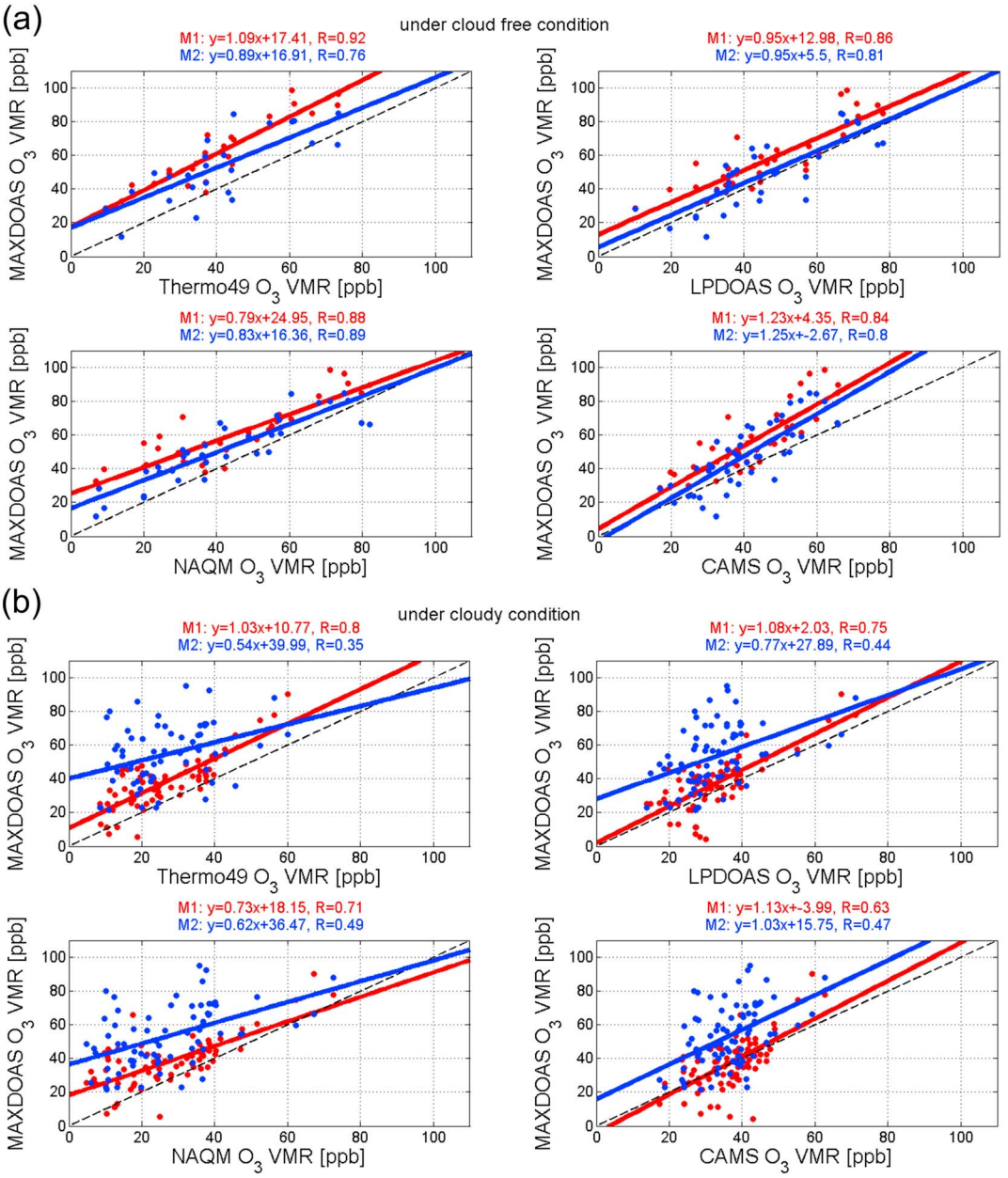

Figure 12. Correlation plots of near-surface (0–200 m) O_3 VMRs retrieved from the MPIC MAX-DOAS measurements versus four other near-surface O_3 data (from the Thermo49i ozone analyzer, the LP-DOAS, the NAQM O_3 in situ instrument, and the CAMS regional model) for the whole campaign under (a) cloud-free and (b) cloudy sky conditions. The fitted linear regression lines and the corresponding equations and correlation coefficients (*R*) are given in each subfigure. The red and blue colors denote the MAX-DOAS results based on the O_3 $dSCD_{Trop}$ retrieved using method 1 and method 2, respectively.

acquired and shown in Figure 14 (the corresponding scatterplots are shown in Figure S7 in the supporting information), indicating that in general, the consistency between the MAX-DOAS results and the CAMS simulations decreases with increasing altitudes. The relative differences of the O_3 results between MAX-DOAS and the CAMS model indicate that the MAX-DOAS results for method 2 are much higher than those for method 1 and the CAMS model at high altitudes.

In summary, the near-surface O_3 results retrieved from the MAX-DOAS measurements using both methods are reasonably consistent with the other independent O_3 data sets. For method 1 reasonable agreement is also found for higher altitudes. However, a large overestimation of O_3 number densities at high altitudes

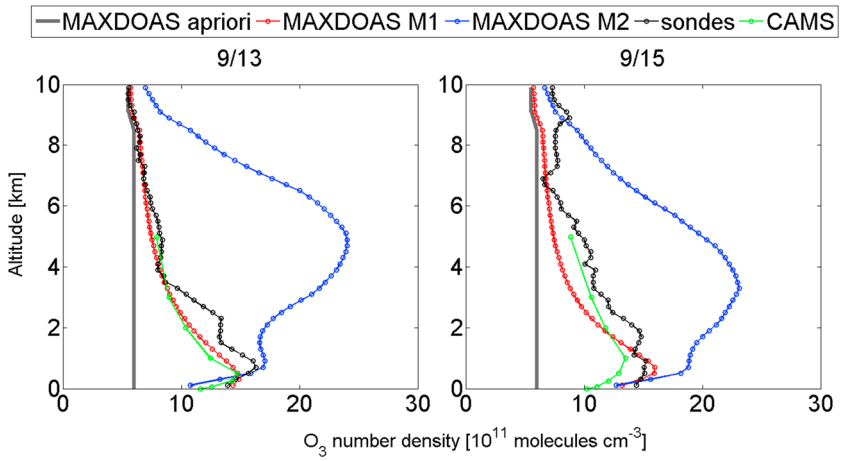

Figure 13. Comparisons of the averaged tropospheric O_3 profiles derived from the MPIC MAX-DOAS measurements based on the O_3 $dSCD_{Trop}$ retrieved using method 1 (red) and method 2 (blue) with results from the CAMS regional model (green), and the ozone sonde measurements (blacks) around noon on two cloud-free days. The a priori profile for the MAX-DOAS O_3 profile inversion is shown as gray line.

(above 1 km) is found for the MAX-DOAS results using method 2. Possible reasons for these deviations are discussed in section 6.2.

6. Investigation of Potential Error Sources of Both Methods

In this section we perform sensitivity studies to assess the effect of several important aspects on the O_3 $dSCD_{Trop}$ retrieved using method 1 and method 2. For method 1 the effects of variations of the stratospheric O_3 profile and RTM simulations of the O_3 $dSCD_{Stra}$ are discussed in section 6.1. For method 2 the effect of RRS and measurement noise are discussed in section 6.2.

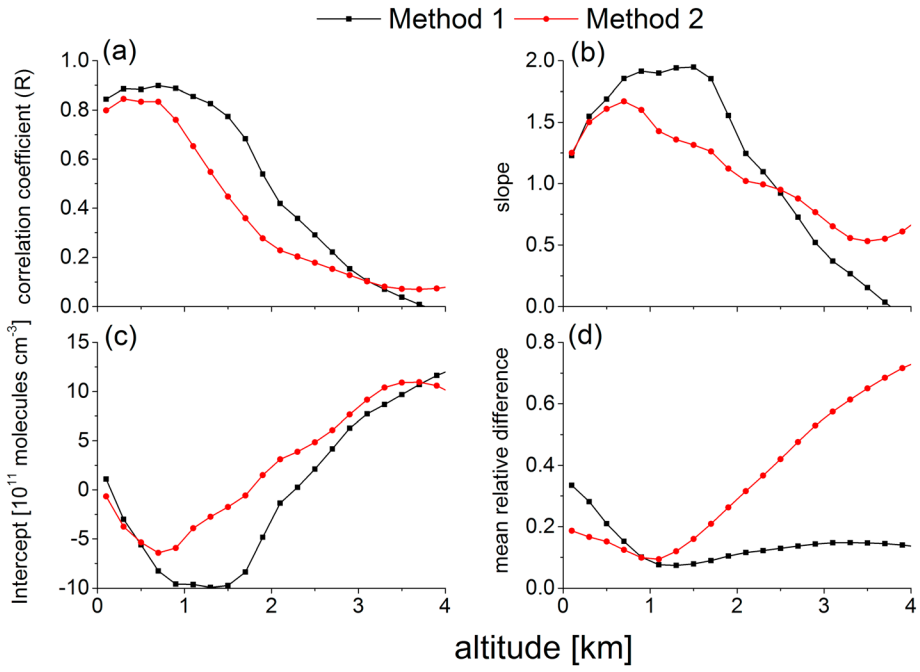

Figure 14. Comparisons of the O_3 number densities retrieved from the MPIC MAX-DOAS measurements versus those from the CAMS regional model at different vertical layers under clear-sky conditions. For the comparisons, (a) correlation coefficients (*R*), (b) slopes, and (c) intercepts derived from linear regressions and (d) mean relative differences are plotted against altitudes.

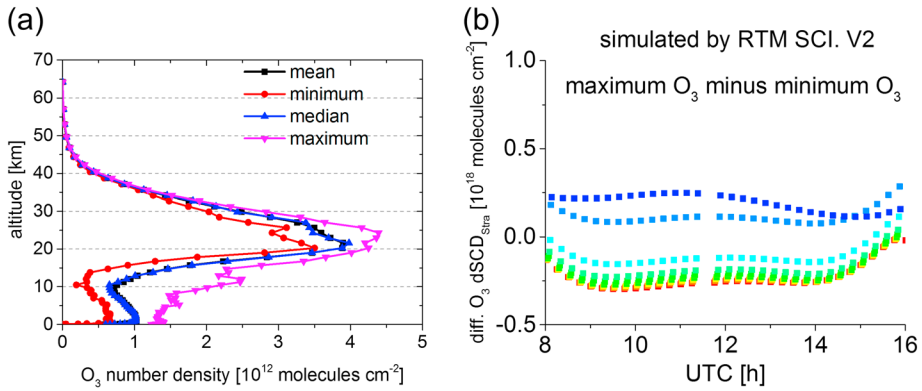

Figure 15. (a) Mean, minimum, median, and maximum of stratospheric O_3 profiles (above 10 km) derived from the CAMS global model during the period of the CINDI-2 campaign. (b) Differences of stratospheric O_3 dSCDs ($dSCD_{Stra}$) simulated by the RTM SCIATRAN v2 for the maximum and minimum O_3 profiles shown in (a). The colors denote the different elevation angles.

6.1. Sensitivity Studies for Method 1

6.1.1. Effects of Variations of the Stratospheric O_3 Profile

For method 1, information about the stratospheric O_3 profile is needed from external sources. In order to evaluate the necessary accuracy of the stratospheric O_3 profiles for the calculation of O_3 $dSCD_{Stra}$, we performed sensitivity tests based on the O_3 profiles from the CAMS global model with a time resolution of 3 h. The maximum, median, minimum, and mean modeled O_3 profiles over the whole CINDI-2 measurement period are shown in Figure 15a. The difference between the O_3 number densities of the maximum and minimum profiles is up to about 1×10^{12} molecules/cm^3 (about 25% of the median profile) at an altitude of about 25 km (the peak O_3 number density). In the next step, the O_3 $dSCD_{Stra}$ are simulated for the maximum and minimum O_3 profiles using the RTM SCIATRAN v2 at a wavelength of 325 nm. In the simulations the same geometries, temperature and pressure profiles, and aerosol properties as for the synthetic spectra with aerosols (see Table 1) are assumed. The differences of the two sets of O_3 $dSCD_{Stra}$ are shown in Figure 15b. They are up to about $\pm 2.5 \times 10^{17}$ molecules/cm^2, depending on the observation geometry. If one fixed stratospheric O_3 profile is used in the retrieval for the whole campaign, the effect of variations of stratospheric O_3 profile on the retrieved O_3 $dSCD_{Trop}$ can be up to 20% for a typical value of the O_3 $dSCD_{Trop}$ of 1×10^{18} molecules/cm^2. Therefore, the closest stratospheric O_3 profiles from the CAMS global model in time to the MPIC MAX-DOAS measurements are used for the calculation of the O_3 $dSCD_{Stra}$ in section 5.1. The validation report for the stratospheric O_3 profiles from the CAMS global model indicates that the relative uncertainty is typically in the range of 10%. Therefore, we estimate the relative uncertainty of the retrieved O_3 $dSCD_{Trop}$ related to the uncertainty of stratospheric O_3 profile to about 10% (corresponding to an absolute uncertainty of about $\pm 1 \times 10^{17}$ molecules/cm^2) during the CINDI-2 campaign.

6.1.2. Effect of Different RT Models on the Stratospheric O_3 dSCDs

For method 1 the O_3 $dSCD_{Stra}$ needs to be calculated based on the dbAMFs simulated by a RTM for individual measurements. The accuracy of these RTM simulations is essential for deriving the correct O_3 $dSCD_{Trop}$. Therefore, we compare the O_3 $dSCD_{Stra}$ calculated by three different RTMs, including SCIATRAN v2, v3, and McArtim v3 (Deutschmann et al., 2011). McArtim is a Monte Carlo RTM based on individual photon trajectories. These simulations provide the most exact representation of the true atmospheric radiative transfer. However, compared to SCIATRAN, the McArtim simulations are much more time consuming. All three RTMs are run for a spherical atmosphere. In the simulations we assume the same scenarios as for the synthetic spectra with aerosols and for O_3 profile 1 (see Table 1). Figure 16a presents the differences of the O_3 $dSCD_{Stra}$ calculated by McArtim and SCIATRAN v2 versus those from SCIATRAN v3. Systematic differences of up to about 2×10^{17} molecules/cm^2 between using SCIATRAN v2 and v3 are found. The differences of O_3 $dSCD_{Stra}$ between McArtim and SCIATRAN v3 are much smaller and are dominated by random noise (due to the photon noise of the Monte Carlo RTM McArtim). In addition to the O_3 $dSCD_{Stra}$ also the O_3 $dSCD_{Trop}$ are compared (right side of Figure 16). Interestingly, the differences are much smaller than for

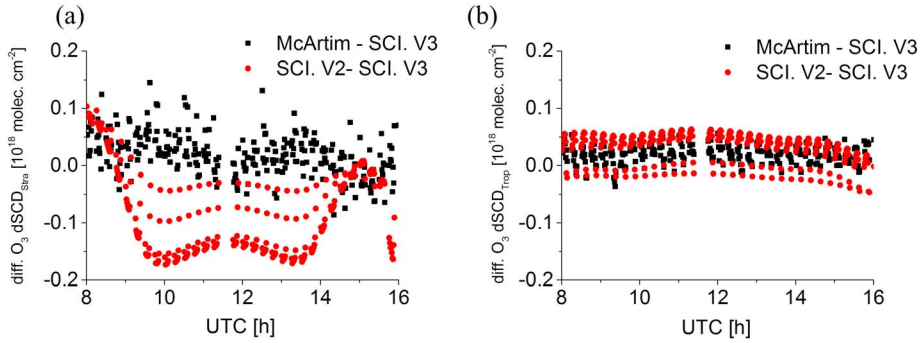

Figure 16. Differences of (a) O_3 $dSCD_{Stra}$ and (b) O_3 $dSCD_{Trop}$ simulated by the RTM McArtim and SCIATRAN v2 compared to those simulated by SCIATRAN v3.

the O_3 $dSCD_{Stra}$ (mostly lower than $\pm 5 \times 10^{16}$ molecules/cm^2). This finding might be caused by the different treatment of the Earth sphericity by the different RTM (Lorente et al., 2017). Because SCIATRAN v2 is used for the simulations of O_3 $dSCD_{Stra}$, the problem could cause the O_3 $dSCD_{Trop}$ for the elevation angle of 1° calculated by the method 1 to be overestimated by up to about 2×10^{17} molecules/cm^2 and further induce the overestimation of O_3 number densities near the surface by about 2×10^{11} molecules/cm^3 (O_3 VMR of about 10 ppb) with an assumption of effective light path of about 10 km. The estimated overestimation of the O_3 number density (and O_3 VMRs) near the surface is consistent with the differences of the retrieved near-surface O_3 values from the MPIC MAX-DOAS between method 1 and method 2 shown in Figure 12a (and Figure 14). In addition, although SCIATRAN v2 probably has problem on the simulations in the stratosphere, because only simulations of tropospheric air mass factors are used in the PriAM for the profile inversion of tropospheric O_3, it is not necessary to change from SCIATRAN v2 to SCIATRAN v3. However, we plan to implement SCIATRAN v3 in PriAM in the near future, because v2 is not officially supported any more by the developer. It needs to be noted that some validation activities have to be done for the new version of PriAM with SCIATRAN v3 before it is applied to data analysis.

6.2. Sensitivity Studies for Method 2

6.2.1. Correction of the Ring Effect

The photons measured by the MAX-DOAS instrument have either undergone only elastic scattering processes or at least one inelastic scattering process. Inelastic scattering includes rotational Raman scattering (RRS), vibrational and vibrational-rotational Raman scattering (Lampel et al., 2015). Only RRS is considered in this study because the contribution of vibrational and vibrational-rotational Raman scattering to the radiances in the wavelength range below 330 nm comes from solar radiances at the wavelengths below 306 nm, which is typically quite low (Lampel et al., 2015, 2018). Therefore, the intensity (I_m) measured by the MAX-DOAS instrument is the sum of the intensity from (only) elastic scattering I_m^{el} and (at least one) RRS I_m^{RRS} (Chance & Spurr, 1997; Grainger & Ring, 1962; Shefov, 1959; Solomon et al., 1987; Wagner et al., 2009):

$$I_m = I_m^{el} + I_m^{RRS} \tag{16a}$$

The DOAS fit is performed in OD space based on Lambert-Beer's law. A reference spectrum I_{FRS}, in analogy to equation (16a), which can be written as

$$I_{FRS} = I_{FRS}^{el} + I_{FRS}^{RRS} \tag{16b}$$

is needed in the DOAS analysis:

$$OD_m^{FRS} = \ln\left(\frac{I_m}{I_{FRS}}\right) = \ln(I_m) - \ln(I_{FRS}) \tag{17}$$

Here OD_m^{FRS} is the differential OD of I_m and I_{FRS}.

By splitting I_m and I_{FRS} into two terms representing elastic scattering and the RRS (equations (16a) and (16b)), equation (17) can be written as

$$\mathrm{OD}_m^{FRS} = \ln\left(\mathrm{I}_m^{el} + \mathrm{I}_m^{RRS}\right) - \ln\left(\mathrm{I}_{FRS}^{el} + \mathrm{I}_{FRS}^{RRS}\right) \tag{18}$$

with I_{FRS}^{el} and I_{FRS}^{RRS} representing the contributions from elastic scattering and RRS, respectively (see equations (16a) and (16b)).

Equation (18) can then be rearranged as following:

$$\begin{aligned}\mathrm{OD}_m^{FRS} &= \ln\left(\mathrm{I}_m^{el}\times\left(1+\frac{\mathrm{I}_m^{RRS}}{\mathrm{I}_m^{el}}\right)\right) - \ln\left(\mathrm{I}_{FRS}^{el}\times\left(1+\frac{\mathrm{I}_{FRS}^{RRS}}{\mathrm{I}_{FRS}^{el}}\right)\right)\\ &= \ln\left(\mathrm{I}_m^{el}\right) + \ln\left(1+\frac{\mathrm{I}_m^{RRS}}{\mathrm{I}_m^{el}}\right) - \ln\left(\mathrm{I}_{FRS}^{el}\right) - \ln\left(1+\frac{\mathrm{I}_{FRS}^{RRS}}{\mathrm{I}_{FRS}^{el}}\right)\\ &= \ln\left(\mathrm{I}_m^{el}\right) - \ln\left(\mathrm{I}_{FRS}^{el}\right) + \ln\left(\frac{\mathrm{I}_m^{el}+\mathrm{I}_m^{RRS}}{\mathrm{I}_m^{el}}\right) - \ln\left(\frac{\mathrm{I}_{FRS}^{el}+\mathrm{I}_{FRS}^{RRS}}{\mathrm{I}_{FRS}^{el}}\right) = \ln\left(\mathrm{I}_m^{el}\right) - \ln\left(\mathrm{I}_{FRS}^{el}\right) + \ln\left(\frac{I_m}{\mathrm{I}_m^{el}}\right) - \ln\left(\frac{I_{FRS}}{\mathrm{I}_{FRS}^{el}}\right)\end{aligned}$$

Finally, it follows

$$\mathrm{OD}_m^{FRS} = \ln\left(\frac{\mathrm{I}_m^{el}}{\mathrm{I}_{FRS}^{el}}\right) + \ln\left(\frac{I_m}{\mathrm{I}_m^{el}}\right) - \ln\left(\frac{I_{FRS}}{\mathrm{I}_{FRS}^{el}}\right) \tag{19}$$

The first term $\ln\left(\frac{\mathrm{I}_m^{el}}{\mathrm{I}_{FRS}^{el}}\right)$ in equation (19) represents elastic scattering; the other terms represent RRS.

In previous studies, a Ring spectrum is usually included in the DOAS fit in order to correct the RRS structures (Solomon et al., 1987). Normally, the Ring spectrum is defined as

$$\mathrm{Ring}_{normal} = \frac{I^{RRS}}{I^{el}} \tag{20}$$

$\mathrm{I}^{\mathrm{RRS}}$ is normally calculated based on a typical I^{el}, which is normally approximated by a measured spectrum of the own instrument or be derived from a high-resolution solar atlas of Kurucz (1984) convoluted to the respective instrumental resolution. Often, an average atmospheric temperature of 250 K is assumed in the calculations of $\mathrm{I}^{\mathrm{RRS}}$. The process of including a Ring_{normal} and possibly an additional Ring spectrum (to account for different broadband wavelength dependencies of I^{el} due to scatterings on cloud particles, or reflection at the Earth's surface based on the study in Wagner et al. (2009)) is referred to as the "normal Ring" procedure in this study. However, the normal Ring procedure is only an approximation of the effect of RRS (see Solomon et al., 1987). The exact RRS spectral structures in the DOAS fits can be exactly represented by the two RRS terms in equation (19):

$$\mathrm{Ring}_{exact} = \ln\left(\frac{I_m}{\mathrm{I}_m^{el}}\right) - \ln\left(\frac{I_{FRS}}{\mathrm{I}_{FRS}^{el}}\right) \tag{21}$$

and referred to as the exact Ring spectrum Ring_{exact} in this study. Note that "exact" refers here to the calculation of the RRS component of the total inelastic scattering as vibrational Raman scattering is ignored in this context. Ring_{normal} is proximately equal with the first-order approximation of the Taylor expansion of Ring_{exact}. And some additional simplifications are done for the calculations of Ring_{normal}, including that the temperature dependence of I^{RRS}, the effects on I^{el} due to scatterings on aerosols and clouds, and absorptions of strong absorbers (e.g., O_3) are not considered.

For the analysis of the synthetic spectra, the Ring_{exact} in equation (21) can be generated using the simulated spectra with and without RRS, because I_m^{el} and I_{FRS}^{el} are equivalent with the intensities of the spectra without RRS. The Ring_{exact} can be generated for individual spectra and be included in the DOAS fit.

We tested the effects of using either the normal Ring spectrum or the exact Ring spectrum on O_3 $dSCD_{Trop}$ (also O_3 $dSCD_{Stra}$ for method 2) based on the synthetic spectra. The differences of the retrieved values compared to the true values (simulated by RTM) are plotted in Figure 17. In addition to the results for the synthetic spectra with RRS, also the results for the synthetic spectra without the RRS are plotted in Figure 17. It can be seen that the O_3 $dSCD_{Trop}$ retrieved using the normal Ring spectra deviate stronger from the true values than those using the exact Ring spectra. The deviations are larger for method 2 than method 1, and for method 2

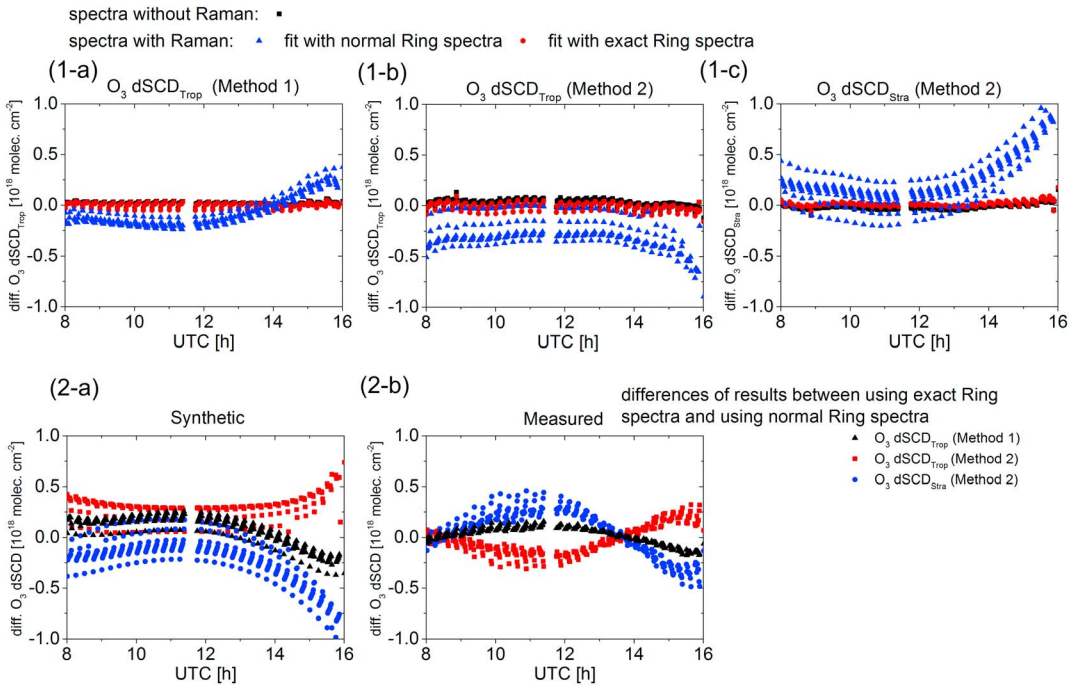

Figure 17. Differences of O_3 $dSCD_{Trop}$ retrieved from the synthetic spectra using (1a) method 1 and (1b) method 2 with respect to the true values (from RTM simulations using SCIATRAN v3) as well as differences of the O_3 $dSCD_{Stra}$ retrieved from the synthetic spectra using (1c) method 2 compared to the true values. In (1a), (1b), and (1c), the black dots denote the results retrieved from the synthetic spectra without RRS; the blue and red dots denote the results retrieved from the synthetic spectra with RRS analyzed with the normal ring or the exact ring spectra, respectively. The differences of the O_3 dSCDs using either the normal ring or the exact ring spectra for the synthetic spectra and the MPIC MAX-DOAS measurements (14 September 2016) are shown in (2a) and (2b), respectively. The black, red, and blue dots indicate the results of the O_3 $dSCD_{Trop}$ using method 1, as well as the O_3 $dSCD_{Trop}$ and $dSCD_{Stra}$ using method 2, respectively.

the deviations of the O_3 $dSCD_{Trop}$ from the true values are anticorrelated with the deviations of the O_3 $dSCD_{Stra}$. In addition, the O_3 $dSCD_{Trop}$ retrieved from the spectra with RRS using the exact Ring spectra still deviate more largely from the true values than the O_3 $dSCD_{Trop}$ retrieved from the spectra without RRS. This finding indicates interferences between the spectral structures of the exact Ring spectrum and the O_3 absorption in the DOAS fit with stronger interferences for method 2 than for method 1. However, the interference effect of the exact Ring spectra is negligible compared to the interference effect of the normal Ring spectra in the DOAS fit.

Considering the significant interference effect of the normal Ring spectra, we also implemented the exact Ring procedure for the real MPIC MAX-DOAS measurements. However, different from the synthetic spectra, the I_m^{el} and I_{FRS}^{el}, which are needed for the calculation of the exact Ring spectra, are not available for the real measurements. Considering that the synthetic spectra are simulated for measurement conditions very close to the real measurements, the exact Ring spectra calculated from the synthetic spectra (with aerosols and for the O_3 profile 1) are used for the analysis of the real measurements. For the real measurements, the differences of the O_3 $dSCD_{Trop}$ (also O_3 $dSCD_{Stra}$ for method 2) retrieved using either the exact Ring spectra or the normal Ring spectra are shown in Figure 17-2a for method 1 and method 2. The same plots are also given for the synthetic spectra in Figure 17-2b. By comparing Figure 17-2a and Figure 17-2b, we can see that the effects of using the two different Ring spectra are quite different for the synthetic spectra and for the real measurements. This finding is probably related to the fact that the "exact" Ring spectra calculated from the synthetic spectra are not fully appropriate for the real measurements. Besides differences of the aerosol properties, also instrumental effects, for instance, stray light, might play a role. The inconsistency of the Ring effects between the synthetic spectra and the real measurements implies that (at least for our measurements), the exact Ring spectra cannot improve the analysis. Therefore, in this study, a normal Ring spectrum is still used in the analysis of the MPIC MAX-DOAS measurements (section 5).

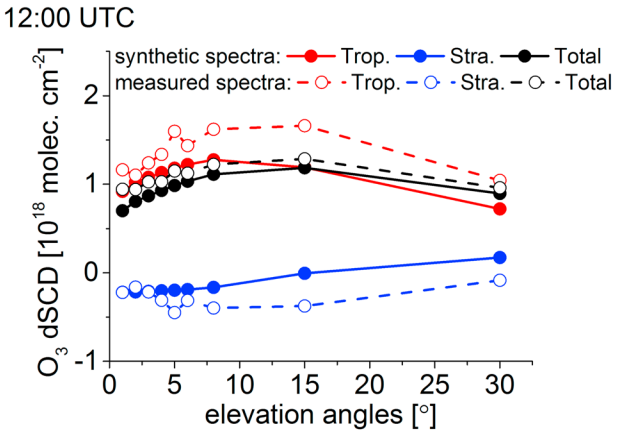

Figure 18. Tropospheric (red), stratospheric (blue), and total (black) O_3 dSCDs as function of the elevation angle retrieved from the synthetic spectra (solid dots) and the MPIC MAX-DOAS measurements (hollow dots) at 12:00 UTC on 14 September 2016.

In summary, we found that for the O_3 analysis, in general, the normal Ring spectra cannot well account for the spectral structures caused by RRS, especially for method 2. For synthetic spectra, the problem can be solved by using the exact Ring spectra. However, the exact Ring spectra are normally not available for real measurements, and even using exact Ring spectra from synthetic spectra for the same measurement conditions did not improve the O_3 results. This discrepancy should be further investigated in a future study. The influence of the Ring effect on the retrieval of the tropospheric dSCDs is stronger for method 2 than for method 1 because the difference of two effective O_3 cross sections is one order smaller than an O_3 cross section.

6.2.2. Unknown Effects Leading to an Overestimation of the Retrieved O_3 Concentration at High Altitudes

An overestimation of the O_3 concentration at high altitudes for method 2 has been seen in Figures 10 and 13. The overestimation is related to larger O_3 $dSCD_{Trop}$ at large elevations for method 2 than for method 1 (see Figure 9). However, this discrepancy is not seen for the synthetic spectra in section 4. The O_3 $dSCD_{Trop}$, O_3 $dSCD_{Stra}$, and the sum of both dSCDs (the total O_3 dSCD) retrieved from the synthetic spectra (with aerosols and for the O_3 profile 1) using method 2 and from the MPIC MAX-DOAS measurements are plotted against the elevation angle in Figure 18 for one elevation sequence at about 12:00 UTC. Similar elevation angle dependencies of the total O_3 dSCD can be found for the synthetic spectra and the real measurements. However, for the O_3 $dSCD_{Trop}$ and O_3 $dSCD_{Stra}$, substantial differences are found between the synthetic spectra and the real measurements. There is no clear explanation for this finding, but we expect that a spectral interference with the Ring effect could be a reason because also the strength of the Ring effect depends on the elevation angle (see Figures 17-1b and 17-1c). In addition, Lampel et al. (2018) demonstrated that MAX-DOAS can measure O_4 absorptions around 328 nm. The O_4 absorption structures could also interfere with the separations of tropospheric and stratospheric O_3. We did the tests by including O_4 absorptions around 328 nm following the suggested procedure in Lampel et al. (2018). The tests indicate that the effects of O_4 absorptions around 328 nm cannot interpret the observed problem of overestimations of O_3 $dSCD_{Trop}$ at large elevation angles. However, the O_4 effects still need to be considered in a further study. In addition, the increase of the number of elevation angles can probably not improve the results, because for method 2, the overestimation of O_3 profile is directly related to the overestimation of the O_3 dSCDs for a large range of elevation angles (between 5 and 15°). In addition, the results of the synthetic study indicate that if the O_3 dSCDs measured at these elevation angles are correct, the tropospheric O_3 profiles can be well retrieved.

6.2.3. Effect of Noise

The effect of measurement noise on the O_3 $dSCD_{Trop}$ retrieved using both methods is tested in this part. For the tests, we generated 100 spectra with a SNR of 3,000 by adding random noise to the synthetic spectrum. O_3 $dSCD_{Trop}$ retrieved from the synthetic spectrum without noise serves as a reference value for the retrieval results of the noisy spectra. The deviations of the O_3 $dSCD_{Trop}$ (also O_3 $dSCD_{Stra}$ for method 2) from the reference value are shown in Figure S8 in the supporting information, indicating that the standard deviation for method 2 is about 1×10^{17} molecules/cm^2, which is much larger than 2.3×10^{16} molecules/cm^2 found for method 1. For method 2, the deviations of the O_3 $dSCD_{Stra}$ are anticorrelated with the deviations of the O_3 $dSCD_{Trop}$ with a correlation coefficient of 0.9, and a slope of -0.81. This noise effect partly explains the larger scatter of the O_3 $dSCD_{Trop}$ retrieved from the MPIC MAX-DOAS measurements using Method 2 compared to method 1 (see Figure 9). Therefore, the applicability of method 2 is also limited by the SNR level of MAX-DOAS instruments.

7. Error Budget

7.1. Error Budgets of Retrievals of Tropospheric O_3 dSCDs

In this section, the error budget of the O_3 $dSCD_{Trop}$ retrieved using both methods is evaluated. The relative errors corresponding to different error sources are given in Figure 19, in which the error sources are sorted into three different groups: errors which only apply to method 1, errors which only apply to method 2, and

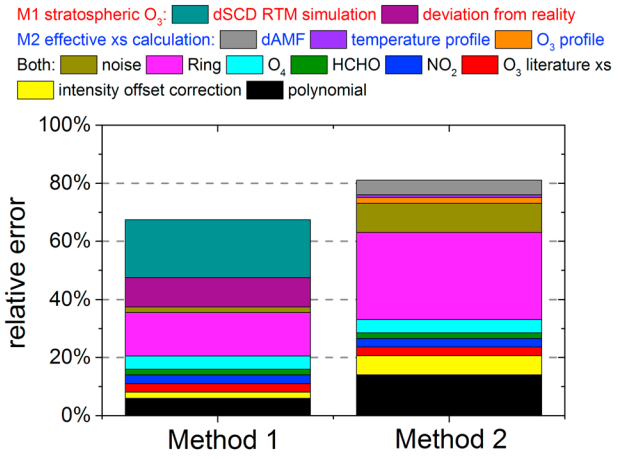

Figure 19. The error budgets of the O_3 $dSCD_{Trop}$ retrieved from the MPIC MAX-DOAS measurements during the CINID-2 campaign using method 1 and method 2. The red and blue marked texts in the legend indicate errors only relevant for method 1 or method 2, respectively. The black marked text indicates errors relevant for both methods.

errors which apply to both methods. For method 1, deviations of stratospheric O_3 profiles (e.g., taken from the CAMS global model) from reality can contribute to the uncertainties of the O_3 $dSCD_{Trop}$ with about 10% (see section 6.1.1). The uncertainties of the O_3 $dSCD_{Trop}$ related to the error of the RTM simulations of the O_3 $dSCD_{Stra}$ are estimated as about 20% (see section 6.1.2). For method 2, errors related to the O_3 profiles, temperature profiles, and dbAMFs (the three items are needed for the calculations of the effective O_3 cross sections) are estimated. The uncertainties related to the O_3 and temperature profiles are about 2 and 1%, respectively, based on the sensitivity study performed in Text S2 in the supporting information. The uncertainty related to the RTM simulations of dbAMFs is estimated at about 5% based on the comparison between the retrieved and simulated true O_3 $dSCD_{Trop}$ for the synthetic spectra in section 4.1. For both methods, the systematic uncertainty of the O_3 cross section can contribute about 3% uncertainty based on Serdyuchenko et al. (2014). To quantify the interference of NO_2, HCHO, O_4 with O_3 in the DOAS fit, we compared the O_3 $dSCD_{Trop}$ retrieved either with or without the cross sections for the other species. The relative differences are then scaled by the typical fit error of these species. The scaled differences indicate upper limits of the uncertainties of O_3 $dSCD_{Trop}$ with respect to interferences with the other species in the DOAS fit. The corresponding uncertainties for NO_2, HCHO, and O_4 are 3, 2, and 4.5%, respectively. The uncertainties of the O_3 $dSCD_{Trop}$ with respect to the Ring effect are estimated as about 15 and 30% for method 1 and method 2, respectively, based on the discussion in section 6.2.1. The uncertainties due to measurement noise can be estimated as about 2% and 10% for method 1 and method 2, respectively, based on the discussion in section 6.2.3. We estimate the uncertainties of O_3 $dSCD_{Trop}$ due to different degrees of the broadband (DOAS) polynomial and the intensity offset correction as 6 and 2% for method 1, and 14 and 6% for method 2, respectively. In summary, the total uncertainties of retrieved O_3 $dSCD_{Trop}$ are calculated from the quadratic sum of the specific errors to about 28 and 36% for method 1 and method 2, respectively, considering the different error sources as independent.

7.2. Error Budgets of the Retrieved Tropospheric O_3 Profiles

In this section, we evaluate the error budget of tropospheric O_3 profiles for both methods based on the MPIC MAX-DOAS measurements. Uncertainties of retrieved profiles can mainly be attributed to the uncertainties of O_3 $dSCD_{Trop}$, artifacts of the PriAM profile inversion, and uncertainties of aerosols. The error due to artifacts of the PriAM profile inversion can be further split into the smoothing error and the inversion convergence error regarding to the cost function (χ^2 in equation (6)). The relative uncertainties for method 1 and method 2 are given in Figures 20a and 20b, respectively, and the absolute uncertainties are given in Figure S9 in the

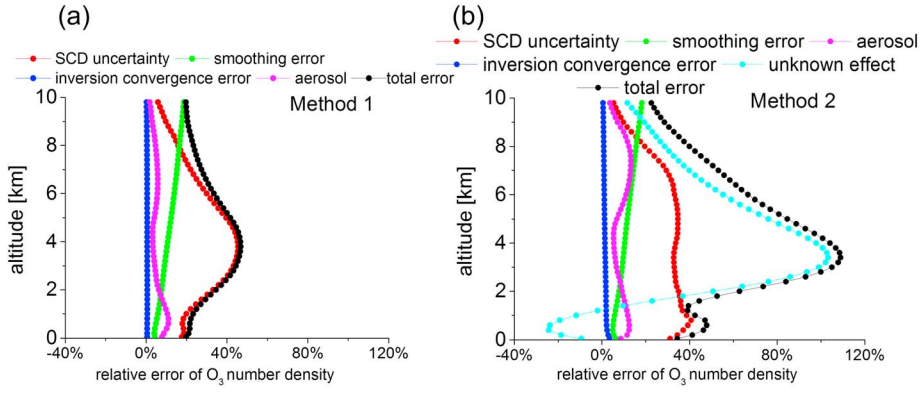

Figure 20. Relative errors of retrieved O_3 profiles from the MPIC MAX-DOAS measurements during the CINDI-2 campaign corresponding to different error sources for (a) method 1 and (b) method 2.

supporting information. The absolute uncertainties show similar patterns as the relative uncertainties. Total uncertainties are calculated from the quadratic sum of the individual errors.

In order to quantify the uncertainties related to the uncertainties of the O_3 $dSCD_{Trop}$, we scaled the O_3 $dSCD_{Trop}$ by ±28 and ±36% (based on the total uncertainty of the O_3 $dSCD_{Trop}$ quantified in section 7.1) for method 1 and method 2, respectively. Then, the tropospheric O_3 profiles are retrieved from the scaled O_3 $dSCD_{Trop}$ and compared with the profiles retrieved from the original O_3 $dSCD_{Trop}$. Similarly, in order to estimate the uncertainties of the retrieved O_3 profiles due to the uncertainties of the aerosol profiles, we retrieve the O_3 profiles with the aerosol profiles scaled by ±20%. Again, the retrieved O_3 profiles are compared to those for the original aerosol profiles. The procedure cannot precisely quantify aerosol effects, because the error budget of aerosol profile retrievals from the MAX-DOAS measurements is not well quantified and the aerosol effects on the O_3 profile retrieval are nonlinear. In addition, for method 2, the unknown effects discussed in section 6.2.2 probably contribute to additional uncertainties of the retrieved O_3 profiles. Therefore, we roughly estimate the uncertainties by comparing the O_3 profiles retrieved from the measured spectra and synthetic spectra around noon.

Figure 20 indicates that the uncertainties of the O_3 $dSCD_{Trop}$ significantly contribute (up to 40% for both methods) to the uncertainties of retrieved O_3 profiles. In addition, the unknown effects for method 2 contribute up to 100% uncertainty, especially at altitudes around 4 km (for which in general the largest total uncertainties for both methods are found). The relative (absolute) uncertainties for method 2 and method 1 are up to about 100% (about 1×10^{12} molecules/cm^3) and 50% (about 6×10^{11} molecules/cm^3), respectively. In addition, following the same approach as for the profiles, the total uncertainties of the retrieved tropospheric O_3 VCD can be estimated. The absolute uncertainties of the retrieved tropospheric O_3 VCD are about 4 and 7×10^{17} molecules/cm^2 for method 1 and method 2, respectively. Assuming a typical tropospheric O_3 VCD of 1×10^{18} molecules/cm^2, the corresponding relative uncertainties are about 40 and 70% for method 1 and method 2, respectively.

8. Discussion and Conclusions

8.1. Discussion on Advantages and Disadvantages of the Two Methods

For method 1, the retrieval of $dSCD_{Trop}$ O_3 depends on the accurate calculation of the O_3 $dSCD_{Stra}$. Errors of the $dSCD_{Stra}$ are caused by possible errors of the RTM simulations and uncertainties of the external data sets of stratospheric O_3 profiles. We also found considerable differences of the O_3 $dSCD_{Stra}$ simulated by different RTM (up to about 10%). In previous studies, the tropospheric dbAMFs simulated by different RTMs for the MAX-DOAS measurement geometries were systematically compared and validated for the retrieval of tropospheric species. However, the validation of stratospheric dbAMF of different RTMs is still rare. Recently, Lorente et al. (2017) demonstrated that differences in the description of the atmosphere's sphericity can lead to significant differences of stratospheric AMFs simulated by different RTMs for satellite observations, especially for large solar zenith angles and viewing zenith angles. Sensitivity studies indicate that a 20% change of the stratospheric O_3 concentration can typically cause a 20% bias of the corresponding O_3 $dSCD_{Trop}$. Therefore, the stratospheric O_3 profiles need to be derived from a credible database, for instance, from climatology, from model simulations, other measurements with a high time resolution, or eventually from the zenith measurements of the MAX-DOAS instrument itself. Algorithms for the retrieval of stratospheric species from zenith measurements of MAX-DOAS instruments during sunset and sunrise have been developed in previous studies (e.g., Hendrick et al., 2011). In addition, in principle, method 1 could also be applied to the O_3 dSCDs retrieved in the visible O_3 Chappuis band (of about 450 to 520 nm). However, in this study, the possibility cannot be tested because the instrument and synthetic spectra do not cover the Chappuis band. It is valuable to test the feasibility in a further study.

For method 2, sensitivity studies demonstrate that RRS can significantly impact the retrieval of the O_3 $dSCD_{Trop}$ and $dSCD_{Stra}$. For the retrieval of the O_3 dSCDs, the use of a normal Ring spectrum, which is an approximation to correct the effect of RRS in the measured spectra, leads to results of insufficient quality causing systematic biases of the retrieved O_3 $dSCD_{Trop}$ of up to 50%. In principle (and for the synthetic spectra), the problem can be solved by using exact Ring spectra in the DOAS fits for individual measurements. However, in this study, the exact Ring spectra calculated from synthetic spectra did not lead to satisfactory

results when applied to real data. Further studies are needed to address this topic. In addition, we found that the O_3 $dSCD_{Trop}$ retrieved from real measurements are systematically overestimated at large elevation angles (eventually leading to significant overestimation of the O_3 concentrations at high altitudes). No clear reason for this finding was identified, but the overestimation might at least partly caused by the problems identified for the Ring effect correction. Another important aspect is the scatter of the O_3 $dSCD_{Trop}$ due to measurement noise. The noise effect on method 2 is 5 times larger than that on method 1 due to the fact that method 2 is sensitive to the differences of two effective O_3 cross sections which are 1 order of magnitude smaller than the total O_3 cross sections used in method 1. Therefore, improvements of the instrumental SNR are essential for method 2. In addition, an accurate temperature profile (especially in the troposphere) needs to be used for the calculation of the effective O_3 cross sections for method 2. A bias in temperatures of 10 K near the surface can cause a bias of retrieved O_3 $dSCD_{Trop}$ by 10%.

In summary, both methods for the retrieval of the O_3 $dSCD_{Trop}$ have their own advantages and disadvantages. The spectral analysis of method 1 is straightforward and stable, but depends on external data sets of stratospheric O_3 profiles and the RTM simulations of stratospheric O_3 dbAMF. Method 2 is independent from external data of stratospheric O_3 profiles, but the spectral analysis is more strongly affected by RRS and measurement noise. It also depends on the differences of the temperatures in the troposphere and stratosphere. If the differences are small, for instance in the polar region, method 2 could not be reasonably applied. Future studies should especially address the imperfections of the Ring effect correction for method 2.

8.2. Conclusions

In this study we developed and applied two methods for the retrieval of tropospheric O_3 profiles from MAX-DOAS measurements. Such retrievals are complicated by the fact that the major fraction of the total O_3 column density is located in the stratosphere. Even if MAX-DOAS measurements are analyzed with sequential Fraunhofer reference spectra, about 30% of the retrieved O_3 dSCDs originate from the stratospheric O_3 absorption. Therefore, a typical MAX-DOAS profile inversion approach cannot work for O_3. The two methods for retrievals of tropospheric profiles and VCD of O_3 developed in this study use different ways to correct for the O_3 $dSCD_{Strat}$ in the retrieval of O_3 $dSCD_{Trop}$. In method 1, the O_3 $dSCD_{Strat}$ is simulated with a RTM using stratospheric O_3 profiles obtained from external data sets and then subtracted from the total O_3 dSCDs retrieved from MAX-DOAS measurements with a sequential FRS to derive O_3 $dSCD_{Trop}$. In method 2, O_3 $dSCD_{Strat}$ and $dSCD_{Trop}$ are separately retrieved using two effective cross sections for tropospheric and stratospheric O_3, respectively. Method 2 makes use of two important properties: (1) the O_3 absorption occurs at significantly different temperatures in the stratosphere and troposphere and (2) the spectral structures of the O_3 cross sections in the Huggins bands are considerably different at different temperatures.

The feasibility of both methods was assessed based on synthetic spectra simulated by RTM. As input parameter for these simulations atmospheric properties (including the O_3 profiles) and viewing geometries similar to the real MAX-DOAS measurement during the CINDI-2 campaign are assumed. Afterward, the tropospheric O_3 profiles are retrieved from O_3 $dSCD_{Trop}$ using the PriAM profile inversion algorithm and compared to the true O_3 profiles used for the generation of the synthetic spectra. In general, the true O_3 profiles are well reproduced by both methods, especially below 2 km. However, the low sensitivity of MAX-DOAS measurements to the upper troposphere and the smoothing effect of the profile inversion make it difficult to reproduce possible steep vertical gradients of the O_3 profiles. The bias of the retrieved O_3 number densities is typically up to 5×10^{11} molecules/cm^2 (generally smaller than 20%). The bias of the retrieved O_3 profiles and the corresponding tropospheric VCD can be attributed to the error of O_3 $dSCD_{Trop}$ retrievals, the configurations of the RTM, and artifacts of the profile inversion algorithm. In summary, tests based on synthetic spectra (without noise) indicate that both methods can well retrieve the O_3 $dSCD_{Trop}$ and the tropospheric O_3 profiles and VCDs if the bAMFs are accurately simulated, and the stratospheric O_3 profiles are well known (for method 1). For method 2, also the Ring effect has to be corrected using exact Ring spectra calculated individually for each measurement.

For real MAX-DOAS measurements during the CINDI-2 campaign, the retrieved near-surface O_3 concentrations for both methods are well consistent with independent measurements. Correlation coefficients (R) are around 0.8 and deviations are smaller than 20% under cloud-free conditions. However, much worse

agreement is found under cloudy conditions, especially for method 2. Moreover, the O_3 concentrations at high altitudes (around 4 km) are significantly overestimated by method 2 (by about 1.5×10^{12} molecules/cm^2) during the whole day. For method 1 only in the afternoon a substantial overestimation (by about 1×10^{12} molecules/cm^2) is found, which is probably related to the extreme geometries with small RAA. Except for measurements at small RAA, method 1 works reasonably well during most of the day.

The total uncertainties of the O_3 $dSCD_{Trop}$ are about 28 and 36% for method 1 and method 2, respectively. For method 1, the dominant error sources are related to uncertainties of the RTM simulations of the O_3 $dSCD_{Stra}$, the Ring effect, and stratospheric O_3 profiles. For method 2, the dominant error sources are related to the Ring effect, the DOAS fit settings, and measurement noise. The total uncertainty of the retrieved tropospheric O_3 profiles depends on altitude and ranges between 20 and 50% (4–6 $\times 10^{11}$ molecules/cm^3) for method 1, and 40–110% (5–11 $\times 10^{11}$ molecules/cm^3) for method 2, respectively. For both methods the largest (relative and absolute) uncertainties are found for altitudes around 4 km. These uncertainties are especially large for method 2 caused by the systematic overestimations of O_3 $dSCD_{Trop}$ at large elevation angles. The total uncertainty of the retrieved tropospheric O_3 VCD is about 40% (4×10^{17} molecules/cm^2) and 70% (7×10^{17} molecules/cm^2) for method 1 and method 2, respectively.

In a separate paper, we plan to compare the tropospheric O_3 dSCDs and profiles retrieved from different MAX-DOAS instruments operated during CINDI-2 campaign using the two methods. The further study can help constrain uncertainties and systematic errors of tropospheric O_3 results due to instrumental problems, that is, stray light, which could also contribute to the overestimation of O_3 values at high altitudes by method 2.

Acknowledgments
Mihalis Vrekoussis and Andreas Hilboll acknowledge support from the DFG-Research Center/Cluster of Excellence "The Ocean in the Earth System-MARUM" and the University of Bremen. The data used are presented in the references, tables, figures, and supporting information.

References

Aliwell, S. R., Van Roozendael, M., Johnston, P. V., Richter, A., Wagner, T., Arlander, D. W., et al. (2002). Analysis for BrO in zenith-sky spectra: An intercomparison exercise for analysis improvement. *Journal of Geophysical Research*, *107*(D14), 4199. https://doi.org/10.1029/2001JD000329

AVANTES enlightening Spectroscopy (2015). Interface Package for 64 BIT Windows Applications, Version 2.3.3.0, USER'S MANUAL, 61.

Bobrowski, N., Hönninger, G., Galle, B., & Platt, U. (2003). Detection of bromine monoxide in a volcanic plume. *Nature*, *423*(6937), 273–276. https://doi.org/10.1038/nature01625

Browell, E. V. (1989). Differential absorption lidar sensing of ozone. *Proceedings of the IEEE*, *77*(3), 419–432. https://doi.org/10.1109/5.24128

Chance, K. V., & Spurr, R. J. (1997). Ring effect studies: Rayleigh scattering, including molecular parameters for rotational Raman scattering, and the Fraunhofer spectrum. *Applied Optics*, *36*(21), 5224–5230.

Clémer, K., Van Roozendael, M., Fayt, C., Hendrick, F., Hermans, C., Pinardi, G., et al. (2010). Multiple wavelength retrieval of tropospheric aerosol optical properties from MAXDOAS measurements in Beijing. *Atmospheric Measurement Techniques*, *3*(4), 863–878. https://doi.org/10.5194/amt-3-863-2010

Danckaert, T., Fayt, C., Van Roozendael, M., De Smedt, I., Letocart, V., Merlaud, A., & Pinardi, G. (2017). QDOAS Software User Manual version 3.2, Belgian Institute for Space Aeronomy (BIRA-IASB).

Deutschmann, T., Beirle, S., Frieß, U., Grzegorski, M., Kern, C., Kritten, L., et al. (2011). The Monte Carlo atmospheric radiative transfer model McArtim: Introduction and validation of Jacobians and 3D features. *Journal of Quantitative Spectroscopy and Radiative Transfer*, *112*(6), 1119–1137. https://doi.org/10.1016/j.jqsrt.2010.12.009

Donner, S. (2016). Mobile MAX-DOAS measurements of the tropospheric formaldehyde column in the Rhein—Main region, (Master Thesis). Institute for Atmospheric Physics of the Johannes Gutenberg University Mainz.

Donner, S., Lampel, J., Shaiganfar, R., Gu, M., & Wagner T. (2015). Construction and characterisation of a new compact MAX-DOAS instrument—Correction of detector non-linearity, presented at 7th international DOAS workshop, Brussels, Belgium.

Eskes, H., Huijnen, V., Arola, A., Benedictow, A., Blechschmidt, A. M., Botek, E., et al. (2015). Validation of reactive gases and aerosols in the MACC global analysis and forecast system. *Geoscientific Model Development*, *8*(11), 3523–3543. https://doi.org/10.5194/gmd-8-3523-2015

Eskes, H. J., Brinksma, E. J., Veefkind, J. P., De Haan, J. F., & Valks, P. J. M. (2005). Retrieval and validation of ozone columns derived from measurements of SCIAMACHY on Envisat. *Atmospheric Chemistry and Physics Discussions*, *5*(4), 4429–4475. https://doi.org/10.5194/acpd-5-4429-2005

Frieß, U., Baltink, H. K., Beirle, S., Clémer, K., Hendrick, F., Henzing, B., et al. (2016). Intercomparison of aerosol extinction profiles retrieved from MAX-DOAS measurements. *Atmospheric Measurement Techniques*, *9*(7), 3205–3222. https://doi.org/10.5194/amt-9-3205-2016

Frieß, U., Monks, P. S., Remedios, J. J., Rozanov, A., Sinreich, R., Wagner, T., & Platt, U. (2006). MAX-DOAS O_4 measurements: A new technique to derive information on atmospheric aerosols: 2. Modeling studies. *Journal of Geophysical Research*, *111*, D14203. https://doi.org/10.1029/2005JD006618

Frieß, U., Sihler, H., Sander, R., Pöhler, D., Yilmaz, S., & Platt, U. (2011). The vertical distribution of BrO and aerosols in the Arctic: Measurements by active and passive differential optical absorption spectroscopy. *Journal of Geophysical Research*, *116*, D00R04. https://doi.org/10.1029/2011JD015938

Grainger, J. F., & Ring, J. (1962). Anomalous Fraunhofer line profiles. *Nature*, *193*(4817), 762. https://doi.org/10.1038/193762a0

Hartl, A., & Wenig, M. O. (2013). Regularisation model study for the least-squares retrieval of aerosol extinction time series from UV/VIS MAX-DOAS observations for a ground layer profile parameterisation. *Atmospheric Measurement Techniques*, *6*(8), 1959–1980. https://doi.org/10.5194/amt-6-1959-2013

Hendrick, F., Pommereau, J. P., Goutail, F., Evans, R. D., Ionov, D., Pazmino, A., et al. (2011). NDACC/SAOZ UV-visible total ozone measurements: Improved retrieval and comparison with correlative ground-based and satellite observations. *Atmospheric Chemistry and Physics*, *11*(12), 5975–5995. https://doi.org/10.5194/acp-11-5975-2011

Hönninger, G., Friedeburg, C. V., & Platt, U. (2004). Multi axis differential optical absorption spectroscopy (MAX-DOAS). *Atmospheric Chemistry and Physics*, *4*(1), 231–254. https://doi.org/10.5194/acp-4-231-2004

Hönninger, G., & Platt, U. (2002). Observations of BrO and its vertical distribution during surface ozone depletion at alert. *Atmospheric Environment*, *36*(15–16), 2481–2489. https://doi.org/10.1016/S1352-2310(02)00104-8

Hoogen, R., Rozanov, V. V., & Burrows, J. P. (1999). Ozone profiles from GOME satellite data: Algorithm description and first validation. *Journal of Geophysical Research*, *104*(D7), 8263–8280. https://doi.org/10.1029/1998JD100093

Horbanski, M. (2016). Emissions and distribution of reactive iodine from seaweed in coastal regions—Investigations using new mobile and in-situ DOAS techniques (doctoral dissertation). Ruprecht-Karls-Universitat Heidelberg. https://doi.org/10.11588/heidok.00020106.

Hough, A. M., & Derwent, R. G. (1990). Changes in the global concentration of tropospheric ozone due to human activities. *Nature*, *344*(6267), 645–648. https://doi.org/10.1038/344645a0

Inness, A., Blechschmidt, A. M., Bouarar, I., Chabrillat, S., Crepulja, M., Engelen, R. J., et al. (2015). Data assimilation of satellite-retrieved ozone, carbon monoxide and nitrogen dioxide with ECMWF's composition—IFS. *Atmospheric Chemistry and Physics*, *15*(9), 5275–5303. https://doi.org/10.5194/acp-15-5275-2015

Irie, H., Kanaya, Y., Akimoto, H., Iwabuchi, H., Shimizu, A., & Aoki, K. (2008). First retrieval of tropospheric aerosol profiles using MAX-DOAS and comparison with lidar and sky radiometer measurements. *Atmospheric Chemistry and Physics*, *8*(2), 341–350. https://doi.org/10.5194/acp-8-341-2008

Irie, H., Takashima, H., Kanaya, Y., Boersma, K. F., Gast, L., Wittrock, F., et al. (2011). Eight-component retrievals from ground-based MAX-DOAS observations. *Atmospheric Measurement Techniques*, *4*(6), 1027–1044. https://doi.org/10.5194/amt-4-1027-2011

Kurucz, R. L. (1984). Solar flux atlas from 296 to 1300 nm. In *National Solar Observatory Atlas* (Vol. 1, pp. 435–436). Cambridge, Mass: Harvard University.

Lampel, J., Frieß, U., & Platt, U. (2015). The impact of vibrational Raman scattering of air on DOAS measurements of atmospheric trace gases. *Atmospheric Measurement Techniques*, *8*(9), 3767–3787. https://doi.org/10.5194/amt-8-3767-2015

Lampel, J., Wang, Y., Hilboll, A., Beirle, S., Sihler, H., Puķīte, J., et al. (2017). The tilt effect in DOAS observations. *Atmospheric Measurement Techniques*, *10*(12), 4819–4831. https://doi.org/10.5194/amt-10-4819-2017

Lampel, J., Zielcke, J., Schmitt, S., Pöhler, D., Frieß, U., Platt, U., & Wagner, T. (2018). Detection of O_4 absorption around 328 and 419 nm in measured atmospheric absorption spectra. *Atmospheric Chemistry and Physics*, *18*(3), 1671–1683.

Lenschow, D. H., Delany, A. C., Stankov, B. B., & Stedman, D. H. (1980). Airborne measurements of the vertical flux of ozone in the boundary layer. *Boundary-Layer Meteorology*, *19*(2), 249–265. https://doi.org/10.1007/BF00117223

Li, X., Brauers, T., Hofzumahaus, A., Lu, K., Li, Y. P., Shao, M., et al. (2013). MAX-DOAS measurements of NO_2, HCHO and CHOCHO at a rural site in southern China. *Atmospheric Chemistry and Physics*, *13*(4), 2133–2151. https://doi.org/10.5194/acp-13-2133-2013

Li, X., Brauers, T., Shao, M., Garland, R. M., Wagner, T., Deutschmann, T., & Wahner, A. (2010). MAX-DOAS measurements in southern China: Retrieval of aerosol extinctions and validation using ground-based in-situ data. *Atmospheric Chemistry and Physics*, *10*(5), 2079–2089. https://doi.org/10.5194/acp-10-2079-2010

Logan, J. A. (1985). Tropospheric ozone: Seasonal behavior, trends, and anthropogenic influence. *Journal of Geophysical Research*, *90*(D6), 10463–10482. https://doi.org/10.1029/JD090iD06p10463

London, J., & Liu, S. C. (1992). Long-term tropospheric and lower stratospheric ozone variations from ozonesonde observations. *Journal of Atmospheric and Terrestrial Physics*, *54*(5), 599–625. https://doi.org/10.1016/0021-9169(92)90100-Y

Lorente, A., Boersma, K. F., Yu, H., Dörner, S., Hilboll, A., Richter, A., et al. (2017). Structural uncertainty in air mass factor calculation for NO_2 and HCHO satellite retrievals. *Atmospheric Measurement Techniques*, *10*(3), 759–782. https://doi.org/10.5194/amt-10-759-2017

Marécal, V., Peuch, V. H., Andersson, C., Andersson, S., Arteta, J., Beekmann, M., et al. (2015). A regional air quality forecasting system over Europe: The MACC-II daily ensemble production. *Geoscientific Model Development*, *8*(9), 2777–2813. https://doi.org/10.5194/gmd-8-2777-2015

Marquard, L. C., Wagner, T., & Platt, U. (2000). Improved air mass factor concepts for scattered radiation differential optical absorption spectroscopy of atmospheric species. *Journal of Geophysical Research*, *105*(D1), 1315–1327. https://doi.org/10.1029/1999JD900340

McPeters, R. D., Bhartia, P. K., Krueger, A. J., Herman, J. R., Schlesinger, B. M., Wellemeyer, C. G., et al. (1996). Nimbus-7 total ozone mapping spectrometer (TOMS) data products user's guide.

Meller, R., & Moortgat, G. K. (2000). Temperature dependence of the absorption cross sections of formaldehyde between 223 and 323K in the wavelength range 225–375 nm. *Journal of Geophysical Research*, *105*, 7089–7101.

Munro, R., Siddans, R., Reburn, W. J., & Kerridge, B. J. (1998). Direct measurement of tropospheric ozone distributions from space. *Nature*, *392*(6672), 168–171. https://doi.org/10.1038/32392

Neu, J. L., Worden, H. M., Kulawik, S. S., Paynel, V. H., Oetjen, H., Walker T., et al. (2017). Understanding differences in satellite records of tropospheric ozone over the past decade, Presented at *EUMETSAT Meteorological Satellite Conference*, Rome, Italy.

Newchurch, M. J., Kuang, S., Leblanc, T., Alvarez, R. J., Langford, A. O., Senff, C. J., et al. (2016). TOLNET—A tropospheric ozone lidar profiling network for satellite continuity and process studies. In B. Gross, F. Moshary, & M. Arend (Eds.), *The 27th International Laser Radar Conference (ILRC 27), EPJ Web of Conferences* (Vol. 119, 20001). New York: EDP Sciences. https://doi.org/10.1051/epjconf/201611920001

Oetjen, H., Payne, V. H., Neu, J. L., Kulawik, S. S., Edwards, D. P., Eldering, A., et al. (2016). A joint data record of tropospheric ozone from Aura-TES and MetOp-IASI. *Atmospheric Chemistry and Physics*, *16*(15), 10229–10239. https://doi.org/10.5194/acp-16-10229-2016

Paur, R. J., & Bass, A. M. (1985). The ultraviolet cross-sections of ozone: II. Results and temperature dependence. In *Atmospheric Ozone* (pp. 611–616). Dordrecht: Springer. https://doi.org/10.1007/978-94-009-5313-0_121

Platt, U., & Stutz, J. (2008). Differential absorption spectroscopy. In *Differential Optical Absorption Spectroscopy* (pp. 135–174). Berlin, Heidelberg: Springer. https://doi.org/10.1007/978-3-540-75776-4_6

Pöhler, D., Vogel, L., Frieß, U., & Platt, U. (2010). Observation of halogen species in the Amundsen gulf, Arctic, by active long-path differential optical absorption spectroscopy. *Proceedings of the National Academy of Sciences*, *107*(15), 6582–6587. https://doi.org/10.1073/pnas.0912231107

Puķīte, J., Kühl, S., Deutschmann, T., Platt, U., & Wagner, T. (2010). Extending differential optical absorption spectroscopy for limb measurements in the UV. *Atmospheric Measurement Techniques*, *3*(3), 631–653. https://doi.org/10.5194/amt-3-631-2010

Puķīte, J., & Wagner, T. (2016). Quantification and parametrization of non-linearity effects by higher-order sensitivity terms in scattered light differential optical absorption spectroscopy. *Atmospheric Measurement Techniques*, *9*(5), 2147–2177. https://doi.org/10.5194/amt-9-2147-2016

Richter, A. (1997). Absorptionsspektroskopische Messungen stratosphärischer Spurengase über Bremen, 53N, Ph.D. thesis, University of Bremen, Bremen, Germany.

Rodgers, C. D. (2000). *Inverse Methods for Atmospheric Sounding, Theory and Practice*, *Series on Atmospheric, Oceanic and Planetary Physics*. Singapore: World Scientific.

Rozanov, A., Rozanov, V., Buchwitz, M., Kokhanovsky, A., & Burrows, J. P. (2005). SCIATRAN 2.0—A new radiative transfer model for geophysical applications in the 175–2400 nm spectral region. *Advances in Space Research*, *36*(5), 1015–1019. https://doi.org/10.1016/j.asr.2005.03.012

Rozanov, V. V., Rozanov, A. V., Kokhanovsky, A. A., & Burrows, J. P. (2014). Radiative transfer through terrestrial atmosphere and ocean: Software package SCIATRAN. *Journal of Quantitative Spectroscopy and Radiative Transfer*, *133*, 13–71. https://doi.org/10.1016/j.jqsrt.2013.07.004

Seinfeld, J. H., & Pandis, S. N. (2016). *Atmospheric Chemistry and Physics: From Air Pollution to Climate Change*. New York: John Wiley & Sons.

Serdyuchenko, A., Gorshelev, V., Weber, M., Chehade, W., & Burrows, J. P. (2014). High spectral resolution ozone absorption cross-sections—Part 2: Temperature dependence. *Atmospheric Measurement Techniques*, *7*(2), 625–636. https://doi.org/10.5194/amt-7-625-2014

Shefov, N. N. (1959). Spectroscopic, photoelectric, and radar investigations of the aurora and the nightglow. *Izd Akad Nauk*, *1*(25).

Solomon, S., Schmeltekopf, A. L., & Sanders, R. W. (1987). On the interpretation of zenith sky absorption measurements. *Journal of Geophysical Research*, *92*(D7), 8311–8319. https://doi.org/10.1029/JD092iD07p08311

Spinei, E., Cede, A., Swartz, W. H., Herman, J., & Mount, G. H. (2014). The use of NO_2 absorption cross section temperature sensitivity to derive NO_2 profile temperature and stratospheric–tropospheric column partitioning from visible direct-Sun DOAS measurements. *Atmospheric Measurement Techniques*, *7*(12), 4299–4316. https://doi.org/10.5194/amt-7-4299-2014

Thalman, R. M., & Volkamer, R. (2013). Temperature Dependent Absorption Cross-Sections of O2–O2 collision pairs between 340 and 630 nm and at atmospherically relevant pressure. *Physical Chemistry Chemical Physics*, *15*, 15,371–15,381. https://doi.org/10.1039/c3cp50968k

Van Roozendael, M., Fayt, C., Post, P., Hermans, C., & Lambert, J. C. (2004). Retrieval of tropospheric BrO and NO_2 from UV-visible observations. In *Sounding the Troposphere from Space* (pp. 155–165). Berlin, Heidelberg: Springer. https://doi.org/10.1007/978-3-642-18875-6_19

Vandaele, A. C., Hermans, C., Simon, P. C., Carleer, M., Colin, R., Fally, S., et al. (1998). Measurements of the NO2 absorption cross-section from 42,000 cm-1 to 10,000 cm-1 (238–1000 nm) at 220 K and 294 K. *Journal of Quantitative Spectroscopy and Radiative Transfer*, *59*, 171–184.

Veefkind, J. P., de Haan, J. F., Brinksma, E. J., Kroon, M., & Levelt, P. F. (2006). Total ozone from the ozone monitoring instrument (OMI) using the DOAS technique. *IEEE Transactions on Geoscience and Remote Sensing*, *44*(5), 1239–1244. https://doi.org/10.1109/TGRS.2006.871204

Vlemmix, T., Piters, A. J. M., Berkhout, A. J. C., Gast, L. F. L., Wang, P., & Levelt, P. F. (2011). Ability of the MAX-DOAS method to derive profile information for NO_2: Can the boundary layer and free troposphere be separated? *Atmospheric Measurement Techniques*, *4*(12), 2659–2684. https://doi.org/10.5194/amt-4-2659-2011

Vlemmix, T., Piters, A. J. M., Stammes, P., Wang, P., & Levelt, P. F. (2010). Retrieval of tropospheric NO_2 using the MAX-DOAS method combined with relative intensity measurements for aerosol correction. *Atmospheric Measurement Techniques*, *3*(5), 1287–1305. https://doi.org/10.5194/amt-3-1287-2010

Wagner, T., Apituley, A., Beirle, S., Dörner, S., Friess, U., Remmers, J., & Shaiganfar, R. (2014). Cloud detection and classification based on MAX-DOAS observations. *Atmospheric Measurement Techniques*, *7*(5), 1289–1320. https://doi.org/10.5194/amt-7-1289-2014

Wagner, T., Beirle, S., Brauers, T., Deutschmann, T., Frieß, U., Hak, C., et al. (2011). Inversion of tropospheric profiles of aerosol extinction and HCHO and NO_2 mixing ratios from MAX-DOAS observations in Milano during the summer of 2003 and comparison with independent data sets. *Atmospheric Measurement Techniques*, *4*(12), 2685–2715. https://doi.org/10.5194/amt-4-2685-2011

Wagner, T., Beirle, S., & Deutschmann, T. (2009). Three-dimensional simulation of the ring effect in observations of scattered sun light using Monte Carlo radiative transfer models. *Atmospheric Measurement Techniques*, *2*(1), 113–124. https://doi.org/10.5194/amt-2-113-2009

Wagner, T., Beirle, S., Remmers, J., Shaiganfar, R., & Wang, Y. (2016). Absolute calibration of the colour index and O_4 absorption derived from multi AXis (MAX-) DOAS measurements and their application to a standardised cloud classification algorithm. *Atmospheric Measurement Techniques*, *9*(9), 4803–4823. https://doi.org/10.5194/amt-9-4803-2016

Wagner, T., Burrows, J. P., Deutschmann, T., Dix, B., Friedeburg, C. V., Frieß, U., et al. (2007). Comparison of box-air-mass-factors and radiances for multiple-axis differential optical absorption spectroscopy (MAX-DOAS) geometries calculated from different UV/Visible radiative transfer models. *Atmospheric Chemistry and Physics*, *7*(7), 1809–1833. https://doi.org/10.5194/acp-7-1809-2007

Wagner, T., Dix, B. V., Friedeburg, C. V., Frieß, U., Sanghavi, S., Sinreich, R., & Platt, U. (2004). MAX-DOAS O4 measurements: A new technique to derive information on atmospheric aerosols—Principles and information content. *Journal of Geophysical Research*, *109*, D22205. https://doi.org/10.1029/2004JD004904

Wang, Y., de Vries, M. P., Xie, P. H., Beirle, S., Dörner, S., Remmers, J., et al. (2015). Cloud and aerosol classification for 2.5 years of MAX-DOAS observations in Wuxi (China) and comparison to independent data sets. *Atmospheric Measurement Techniques*, *8*(12), 5133–5156. https://doi.org/10.5194/amt-8-5133-2015

Wang, Y., Lampel, J., Xie, P., Beirle, S., Ang, L., Wu, D., & Wagner, T. (2017). Ground-based MAX-DOAS observations of tropospheric aerosols, NO_2, SO_2 and HCHO in Wuxi, China, from 2011 to 2014. *Atmospheric Chemistry and Physics*, *17*(3), 2189–2215. https://doi.org/10.5194/acp-17-2189-2017

Wang, Y., Li, A., Xie, P. H., Chen, H., Mou, F. S., Xu, J., et al. (2013b). Measuring tropospheric vertical distribution and vertical column density of NO_2 by multi-axis differential optical absorption spectroscopy. *Acta Physica Sinica*, *16*, 200705. https://doi.org/10.7498/aps.62.200705

Wang, Y., Li, A., Xie, P. H., Chen, H., Xu, J., Wu, F. C., et al. (2013a). Retrieving vertical profile of aerosol extinction by multi-axis differential optical absorption spectroscopy. *Acta Physica Sinica*, *16*, 180705. https://doi.org/10.7498/aps.62.180705

Wittrock, F. (2006). The retrieval of oxygenated volatile organic compounds by remote sensing techniques (Doctoral dissertation). University of Bremen, Bremen, Germany, available at: http://www.doas-bremen.de/paper/diss_wittrock_06.pdf (last access: December 2015).

Wittrock, F., Oetjen, H., Richter, A., Fietkau, S., Medeke, T., Rozanov, A., & Burrows, J. P. (2004). MAX-DOAS measurements of atmospheric trace gases in Ny-Ålesund-Radiative transfer studies and their application. *Atmospheric Chemistry and Physics*, *4*(4), 955–966. https://doi.org/10.5194/acp-4-955-2004

Yilmaz, S. (2012). Retrieval of atmospheric aerosol and trace gas vertical profiles using multi-axis differential optical absorption spectroscopy (Doctoral Dissertation). University of Heidelberg, Germany.

Young, P. J., Naik, V., Fiore, A. M., Gaudel, A., Guo, J., Lin, M. Y., et al. (2018). Tropospheric ozone assessment report: Assessment of global-scale model performance for global and regional ozone distributions, variability, and trends. *Elementa: Science of the Anthropocene*, *6*(1). https://doi.org/10.1525/elementa.265

Ziemke, J. R., Chandra, S., Duncan, B. N., Froidevaux, L., Bhartia, P. K., Levelt, P. F., & Waters, J. W. (2006). Tropospheric ozone determined from Aura OMI and MLS: Evaluation of measurements and comparison with the global modeling initiative's chemical transport model. *Journal of Geophysical Research*, *111*, D19303. https://doi.org/10.1029/2006JD007089